

CALOTRITON: A convective boundary layer height estimation algorithm from UHF wind profiler data

Alban Philibert^{1,2}, Marie Lothon², Julien Amestoy³, Pierre-Yves Meslin¹, Solène Derrien², Yannick Bezombes², Bernard Campistron², Fabienne Lohou², Antoine Vial², Guylaine Canut-Rocafort⁴, Joachim Reuder⁵, and Jennifer Brooke⁶

¹Institut de Recherche en Astrophysique et Planétologie, Université de Toulouse, CNRS, UPS, France

²Laboratoire d'Aérodynamique, Université de Toulouse, CNRS, UPS, France

³CEA, DAM, DIF, F-91297, Arpajon-Cédex, France

⁴CNRM-Université de Toulouse, Météo-France/CNRS, Toulouse, France

⁵Geophysical Institute, and Bergen Offshore Wind Centre, University of Bergen, and Bjerknes Center for Climate Research, Bergen, Norway

⁶Met Office, FitzRoy Way, Exeter, EX1 3PB, UK

Correspondence: Marie LOTHON (marie.lothon@aero.obs-mip.fr)

Abstract.

Long ~~series of observation of the~~ time series of observations of atmospheric dynamics and composition are collected at the French Pyrenean Platform for the Observation of the Atmosphere (P2OA). Planetary boundary layer depth is a key variable of the climate system, but it remains difficult to estimate and analyse statistically ~~by use of long series~~. In order to obtain reliable estimates of the convective boundary layer height (Z_i) and to allow long-term series analyses, a new restitution algorithm, named CALOTRITON, has been developed. ~~It is~~ based on the observations of a Ultra High Frequency (UHF) radar wind profiler (RWP) from P2OA, with the help of other instruments for evaluation. Z_i estimates are based on the principle that the top of the convective boundary layer is associated with both a marked inversion and a decrease of turbulence. Those two criteria are respectively manifested by larger RWP reflectivity and smaller vertical velocity Doppler spectral width. With this in mind, we introduce a new UHF-deduced dimensionless parameter which weights the air refractive index coefficient with the inverse of vertical velocity standard deviation to the power x . We then search for the most appropriate local maxima of this parameter for Z_i estimates, with defined criteria and constraints, ~~like such as~~ temporal continuity. Given that Z_i should correspond to fair weather cloud base height, we use ceilometer data to optimize our choice of the power x , and find that $x = 3$ ~~gives provides~~ the best comparisons ~~results~~. The estimates of Z_i by CALOTRITON are evaluated using different Z_i estimates deduced from radiosounding, according to different definitions. The comparison shows excellent results with a regression coefficient of up to 0.96 and a root mean square error of ~~8071~~ m, close to the vertical resolution of the UHF RWP of 75 m, when conditions are optimal. In more complex situations, that is when the atmospheric vertical structure is itself particularly ambiguous, secondary retrievals allow us to identify potential thermal internal boundary layers or residual layers, and help to qualify the Z_i estimations. Frequent estimate errors are nevertheless observed, ~~for example~~ when Z_i is below the UHF RWP first reliable gate, ~~but also at the end of the day, or~~ when the boundary layer begins its transition to a stable ~~nighttime nocturnal~~ boundary layer.

1 Introduction

1.1 ~~Z_i definitions in CBL and associated instrumental~~ Instrumental techniques for convective boundary layer retrieval

25 The convective boundary layer (CBL) is defined as the lower layer of the troposphere where buoyancy mainly drives turbulence (Stull, 1988). CBL top (Z_i depth (Z_i)) is a key variable in air quality since pollutants, dust, smoke, ... emitted at the surface are mixed within this depth by dynamical and thermal turbulence. It is also a key variable for numerical weather predictions and climate models; the climate system, for its role in modulating energy, water and trace species exchange at the interface between surface and free atmosphere. For this reason, it has significant applications in air quality, numerical weather predictions, climate models, and in more applied sectors such as renewable energy production. There are challenges in understanding the role of the convective boundary layer over heterogeneous surface, in complex terrain, coastal areas, polar regions, for surface/atmospheric exchange, transport and mesoscale circulation; all of which require a comprehensive estimate of the CBL depth. Although, it remains difficult to accurately and exhaustively quantify in the real world both in terms of the spatial and temporal variability, due to its complexity.

35 Instrumental techniques for Z_i retrieval are numerous, and have lead to an abundance of literature. Kotthaus et al. (2023) propose a recent overview of the CBL top detection measurement techniques, with an exhaustive description of their capabilities and limitations. Here we summarise the most relevant techniques applicable to this study.

There are several definitions of ways to identify Z_i , depending on the points of view, notably based on its characteristic atmospheric processes, which can be used to define different observational techniques. They can be classified in three main approaches: (i) thermodynamically based on the thermodynamical processes, (ii) from the turbulence intensity, based on the turbulent processes, and (iii) from the scalar concentration those based on tracers. Figure 1 schematizes those various definitions, through the vertical profiles of key variables.

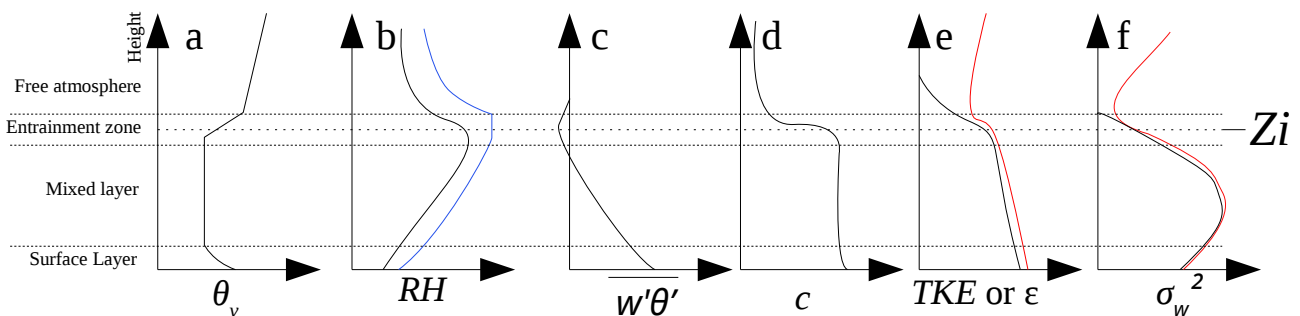


Figure 1. Idealized CBL profiles (black line) of (a) potential temperature, (b) relative humidity (blue line indicates the situation in the presence of clouds), (c) buoyancy flux, (d) scalar concentration, (e) turbulent kinetic energy (TKE) or turbulent dissipation rate (ϵ) and (f) vertical velocity variance (red line indicates the situation in the presence of external forcing).

~~The thermodynamic~~ The thermodynamical approach considers Z_i as the height, from the surface, at which the ~~somital~~ sommital inversion occurs, characterized by strong gradients of temperature and moisture (Fig. 1a, 1b). Several instrumental
45 methods estimate Z_i based on this approach, e. g. :

- the detection of gradients of either potential temperature, relative humidity (RH) or water vapor mixing ratio (e. g. Hen-nemuth and Lammert, 2006).
- the detection of the maximum of relative humidity (Couvreux et al., 2016).
- the so-called parcel method, which considers the potential temperature (or virtual potential temperature) at the surface
50 θ_s , and searches for the height above surface where $\theta = \theta_s$ (Holzworth, 1964), or $\theta = \theta_s + \delta\theta$, where $\delta\theta$ is a small positive variation of surface potential temperature (Seibert et al., 2000) .

In-situ measurements from radiosounding, aircraft or remotely piloted aircraft systems (RPAS) can be used~~–~~, based on this approach. Remote sensing provides an indirect measure of thermodynamical variables, such as, Microwave Radiometers, Raman lidar, or differential absorption lidar. Indirectly related to this approach. Ultra High Frequency (UHF) radar wind profil-
55 ers (RWPs), in L-band remote sensing, are also appropriate devices to detect the ~~Z_i -sommital inversion~~ CBL sommital inversion, which is associated with a significant increase of reflectivity (~~Angevine et al., 1994~~) (White, 1993; Angevine et al., 1994).

~~The turbulence intensity approach considers~~ Approaches based on turbulent processes consider Z_i as the height, from the surface, where turbulence intensity starts to strongly decrease (Fig. 1e). This height is coupled with minimum (and negative) buoyancy flux (Deardorff, 1972) and decrease of vertical velocity variance (Stull, 1988), Turbulent Kinetic Energy (TKE), or
60 TKE dissipation rate (ϵ). Both buoyancy flux and vertical velocity variance reach zero above Z_i . ~~But in case~~, in textbook cases (unforced conditions, clear air). However in cases of external forcing like such as clouds, wind shear ~~, advection, ...~~, or advection, a local minimum can be observed on each profiles (see red line Fig. 1e, 1f). Doppler lidar and UHF RWP give information on the turbulence intensity (Frehlich et al., 2006; Jacoby-Koaly et al., 2002, respectively). The variance of the Doppler velocity (Lothon et al., 2006), or the turbulent kinetic energy dissipation rate (e. g. Frehlich et al., 2006) can be used
65 to detect the CBL top, based on a threshold. Note that studies based on numerical weather predictions models often use TKE as a reference for Z_i determination (Couvreux et al., 2016), and studies based on Large Eddy Simulation often consider the minimum of buoyancy flux (e. g. Pino et al., 2006). This makes those turbulence-based approaches very relevant for model evaluation.

The ~~scalar concentration-tracer-based~~ approach considers Z_i as the height, from the surface, where strong discontinuity is
70 observed in the scalar concentration profiles (Fig. 1d) like aerosol such as aerosol or gas concentration. Optical remote sensing, like e.g. lidar and ceilometers, ~~enable to access to aerosol concentration with measure~~ the optical backscatter coefficient from which aerosol concentration can be inferred (Kotthaus et al., 2023, for an exhausitive list). Wavelet methods are typically used to detect the top of the more loaded CBL (e. g. Haeffelin et al., 2012), where the aerosol concentration abruptly falls from the CBL to the free troposphere (see e. g. Davis et al., 2000, for the use of the Haar-wavelet-based method). The mixing ratio
75 maximum gradient method described above could also be considered as a scalar concentration approach.

Other approaches propose to use the combination of complementary instruments, like Min et al. (2020), with Some approaches use the use of synergy of instruments or methods. The bulk Richardson method (Hanna, 1969), with a threshold on the gradient Richardson, is a combination of wind gradient and potential temperature gradient. The complementarity of instruments is widely used for Z_i estimations. For example, Min et al. (2020) or Turner and Lohnert (2021) use the association of a microwave radiometer with ceilometer. Some studies compare the various methods and instrumental approaches, e.g. Couvreux et al. (2016) or Duncan et al. (2022). The latter discuss the weather conditions for which the various instruments are the most appropriate. In their study, RWP is found to give robust results, with a small bias relative to the radiosoundings, and a decrease of performance in the presence of clouds (due to the presence of turbulence in clouds).

or Raman lidar respectively. Since they are based on different definitions, all the methods mentioned before discussed potentially result in slightly different estimates of Z_i (Caicedo et al., 2017), especially when the observed CBL is not as simple as in a textbook a simple idealised case.

Here In this study, we revisit the methodology of estimating Z_i from UHF RWP measurements, and propose a new complementary algorithm. The advantage of RWP relatively to other remote sensing devices is their ability to measure in all weather types and not limited by cloud types and amount, precipitation or clear-sky conditions. Their height coverage limitation is predominately related due to water vapour content. One known weakness is their sensitivity to bird echoes, which typically occur at nighttime during bird migration events, particularly in spring and autumn. It is usually not a significant issue during daytime convection.

1.2 Motivations and Main objectives

As one of the The multi-instrumented site of the ACTRIS-Fr¹ infrastructure, the Pyrenean Platform for the Observation of the Atmosphere (P2OA² – Lothon et al., 2023) (P2OA³ – Lothon et al., 2023) gathers a comprehensive set of instruments for the monitoring of the atmosphere, all with a sub selection of instrumentation located at the Center for Atmospheric Research (CRA), Campistrous, France in South-West France, close to the Pyrenees mountain ridge. Among them, a UHF RWP has continuously documented the Planetary Boundary Layer measured the boundary layer since 2010. Retrieving the CBL height from this instrument over this ongoing long series would allow from this multi-year time series allows a statistical study of the dynamical processes in this mountainous region, such like: Processes include the influence of plain-mountain circulations, in link with thermally-driven winds; the interaction between mountain waves and boundary layer; and the impact of mesoscale subsidence related to orographic convection. It would also enable This unique dataset enables us to make statistical analysis and climatologies, with applications in for air quality, weather forecasting and climate studies.

*An existing technique partly based by Angevine et al. (1994) was used as a reference for this specific fluid for the estimate of Z_i with this instrument. It is known that this technique gives (Jacoby-Koaly et al., 2002). Angevine et al. (1994) base the estimate of Z_i on the absolute maximum of the air refractive index structure coefficient (C_n^2) which however does not always correspond to the current CBL top, but can correspond to a residual inversion above. To address this, Jacoby-Koaly et al. (2002) attempted to retrieve the local maximum of C_n^2 that could be the most appropriate estimate of Z_i , by use of temporal continuity, and other

¹ACTRIS-Fr is the French component of the European Aerosol, Cloud and Trace Gases Research Infrastructure (ACTRIS), <https://www.actris.fr/>

criteria. This is also the approach of Collaud Coen et al. (2014). Note that C_v^2 reaches local maxima where temperature and humidity show large vertical gradients, but also large wind gradients and turbulence (which induces fluctuations of air refractive index). This technique provides very satisfying results on a case-by-case investigation for fair weather convective conditions without complex vertical structure of the atmosphere (Heo et al., 2000)(Heo et al., 2003; Jacoby-Koaly, 2000). However, this technique is not robust enough for statistical studies based on long series. ~~statistical studies of the time series based on this technique may not be possible without significant errors.~~ One obvious limitation for example, is that it often catches the top of the residual layer in early morning, rather than the top of the ~~new thinner shallower~~ developing CBL top. ~~Here, we propose to improve the method, and develop a new algorithm that would be able to deal with much more general~~ The temporal continuity criteria does not solve this issue. Attributing Z_i as the top of the residual layer during the morning transition potentially leads to large errors. This can also occur in late afternoon, when this method will likely attribute Z_i at the top of the pre-residual layer

2.2 Datasets

In this study, we consider the data of the ~~P2OA UHF RWP to~~ LAERO UHF RWP at the P2OA-CRA from 2015 to 2022, to develop the new CALOTRITON algorithm, ~~for the retrieval of the CBL height throughout the whole 22-year long and ongoing time series of observations~~ also use ~~the data from the P2OA~~ sensible heat flux measurements from a sonic anemometer installed at 30 m on the P2OA-CRA 60m instrument tower, and relative humidity measurements, made at 2 m.

125 ~~Summary of instruments used and datasets~~

~~P2OA observatory 2015-2022 Lothon et al. (to be specified) BLLAST June to July 2011 Saïd (2012) Els Plan, Spain LIAISE July 2021 Lothon and Vial (2022) Capvern, France BLLAST June to July 2011 Garrouste (2011) La Cendrosa, Spain LIAISE July 2021 Vial (2023) P2OA-CRA Lothon (2018)-~~

130 ~~Capvern, France Legain (2011)-~~

~~Els Plan, Spain Price (2023b) La Cendrosa, Spain Garrouste et al. (2022)-~~

~~Remotely Piloted P2OA-CRA Airplane System Capvern, France P2OA observatory 2015-2022 Lohou et al. (to be specified), t-~~

~~BLLAST June to July 2011 Lohou (2017) Els Plan, Spain Price (2023a) La Cendrosa, Spain Canut et al. (2022)-~~

135 ~~CT25k Ceilometer P2OA-CRA P2OA observatory 2016-2019 see Data availability~~

To optimize CALOTRITON parameters, we compare Z_i estimates with cloud base heights (Sect. 3.3) measured by ~~the a~~ CT25k ceilometer from Centre National de Recherche Météorologique (CNRM), installed from December 2016 to December 2019 at P2OA-CRA.

The algorithm results are ~~then~~ validated (see Sect. ~~??5~~) by comparison to in-situ ~~radiosonde and profiles made with radiosonde~~ ~~or~~ Remotely Piloted Airplane System (RPAS) ~~measurements~~ during two intensive ~~measurement campaigns~~ field campaigns: (i) BLLAST (Boundary Layer Late Afternoon and Sunset Turbulence, Lothon et al., 2014), which took place at P2OA-CRA and (ii) LIAISE (Land surface Interactions with the Atmosphere over the Iberian Semi-arid Environment, Boone et al., 2021),

which took place in North-East Spain, close to Lleida. The latter enables us to test CALOTRITON in another meteorological and geographical context than for to that of the long term observational record of P2OAP2OA-CRA, and thus generalize its applicability and use. For both measurement campaigns, the CNRM UHF RWP is used in addition to the P2OA-LAERO UHF RWP which also allows-enables to test the algorithm on a different UHF RWP.

2.2 UHF RWP measurement example

Table 1 summarises the contexts of RWP measurements used and corresponding time period, the location of RWPs, the complementary instrumentation used and their role in this study. The corresponding datasets are listed and referenced in the Data availability section, at the end of the article, with more precision on the specific periods for each instrument.

Table 1. Summary of instruments used and context

~~In this section, we present two study cases to illustrate our motivations to improve the current methods of Z_i retrieval from a UHF RWP: one simple clear sky case (27 Oct 2017) and one more complex case (27 Oct 2017).~~

	P2OA
	BLLAST
	LIAISE

150

The sensible heat flux is calculated on 30 min duration samples with EddyPro software, based on Eddy-Correlation technique. The UHF RWP instruments and data process is detailed in the following.

~~The P2OA-~~

2.2 UHF Radar Wind profiler technical characteristics and data process

155 The LAERO UHF RWP is a 1.274 GHz wind profiler with 5 beams, four oblique beams and one vertical beam. Its main characteristics are detailed-listed in Table 2 (for more details, see Jacoby-Koaly, 2000). It runs alternatively with two modes: one 'low mode' with a pulse width of 500 ns corresponding to a range resolution of 75 m, and a 'high mode' with the pulse width of 2.5 μ s corresponding to a range resolution of 150 m and a slightly better height coverage. For our use here, we only consider the low mode. The maximum height for this mode is usually around 3 km a. g. l., but may be only 500 m or 1000 m
 160 in winter, when dry anticyclonic conditions occur. It can reach 7 or 9 km within deeper clouds and rain. The first gate is 75 m, but with a poor confidence index. We consider the 225 m gate as first gate with very good confidence. The CNRM UHF RWP mainly presents the same characteristics but with a first level with a good confidence index at 300 m.

Table 2. Main characteristics of the P2OA-LAERO UHF RWP (https://p2oa.aeris-data.fr/sedoo_instruments/profileur-de-vent-uhf/).~~The CNRM-UHF RWP present the same characteristics but with a first level with a good confidence index of 300 m.~~

Manufacturer	Degreane
Reference	PCL1300
<u>Emission frequency</u>	<u>1.274 GHz</u>
Number of beams	5 (<u>NWSE+vertical</u> <u>N-W-S-E-vertical</u>)
Transmission Frequency	1274 MHz
Opening Angle	8.5°
Obliques antennas <u>inclinaison</u> <u>Angle</u>	17° to the vertical
Vertical Resolution	75 m
Temporal Resolution	~ 2 <u>minutes</u> <u>min</u>
First level with a good confidence index	225 m
<u>Vertical coverage</u> height	<u>~ 3 km</u>

UHF RWP observations for 27 October 2021 at P2OA-CRA during clear sky: (a) wind speed (WS), (b) wind direction (WD), (c) filtered C_n^2 in log scale, (d) filtered σ_w^2 in log scale, (e) filtered and integrated ε in log scale, (f) integrated $NP3$ in log scale. For all panels, Z_i estimates as described in Sect. 3.2.2 and 3.3.3: $Z_{i\varepsilon}$ (orange line), $Z_{iNP0_{std}}$ (purple line), $Z_{iNP0_{sup}}$ (purple circles), $Z_{iNP3_{std}}$ (green line), $Z_{iNP3_{sub}}$ (green circles); and based on the same ordinate axis (but with different units): short wave down ($W\ m^{-2}$) (black line), sensible heat flux ($decIW\ m^{-2}$) (blue line). The vertical dashed line correspond to the time of the discussed radiosounding.

Figure 4 (panels a to e) shows different parameters measured by the UHF RWP in a clear sky case on 27 October 2021 at P2OA-CRA. The 3 components of the wind are deduced from the Doppler radial velocity of the 5 beams, every 75 m, and every 2 minutes. The first main critical step is to select the meteorological peak from the Doppler spectrum. We use a process developed at LAERO laboratory, which optimize the meteorological peak selection and data coverage, relative to the manufacturer processing. During this phase, an automatic quality control is done, eliminating Doppler spectral erroneous peaks before the wind component calculation. The second step is typical of velocity volume processing technique (Wadteufel and Corbin, 1979), which computes the three wind components from the radial velocity, with minimum least square error. The air refractive index structure coefficient C_n^2 (Fig. 4e) is deduced from the reflectivity as a function of the received power (Doviak and Zrnica, 1993). The vertical velocity variance σ_w^2 (Fig. 4d) is obtained from the spectral half Doppler width of the backscattered signal and allows an estimate of the turbulent kinetic energy (TKE) on the vertical beam, and gives and allows to estimate TKE dissipation rate ε (Fig. 4e) (Cohn and Angevine, 2000; Jacoby-Koaly et al., 2002). Here (Cohn and Angevine, 2000; Jacoby-Koaly et al., 2002). Hereafter, C_n^2 is the median air refractive index structure coefficient over the 5 beams, as a function of and depends on altitude and time. ε is the median TKE dissipation rate over the 5 beams. σ_w is deduced from vertical antenna and corrected for the effect of the horizontal wind within the antenna aperture (Jacoby-Koaly et al., 2002). All those variables are calculated at 2 min time interval.

Figure ?? (panels a to g) compares in-situ measurements of thermodynamical variables measured by radiosondes with the UHF RWP variables at 13:35 UTC, on the same day of UHF RWP observations shown in Fig. 4.

Angevine et al. (1994) propose a CBL top retrieval method based on UHF RWP measurements, by assigning Z_i at the height of the maximum reflectivity for each profile. Figure ??d indeed shows that the maximum reflectivity corresponds well to the CBL top, characterized by a strong gradient of potential temperature and mixing ratio (Fig. ??a and ??b). It indeed shows that σ_w^2 (Fig. ??e) and ε (Fig. ??f) are small at this height, leading to a local minimum. In "ideal" clear days, without external forcing, we would typically not observe significant turbulence above Z_i (Fig. 1e). In this case, forcing is small, with weak wind (Fig. 4a) but the wind shears (Fig. 4b) still generates significant turbulence (Fig. 4e).

Profiles measured by radiosondes and UHF RWP at P2OA-CRA, on 27 October 2021, at 13:35 UTC: (a) potential temperature (black solid line), surface potential temperature + 0.25°C (black dashed line), Z_i from in-situ subjective method (black circle), Z_i from in-situ potential temperature gradient method (black asterisk), $Z_{i_{NP0_{std}}}$ (purple 'x'), $Z_{i_{NP0_{sup}}}$ (purple '+'), $Z_{i_{NP3_{std}}}$ (green 'x'), $Z_{i_{NP3_{sub}}}$ (green '+'), $Z_{i_{\varepsilon}}$ (orange '+'); (b) mixing ratio (black line) and relative humidity (blue line), Z_i from in-situ mixing ratio gradient method (black asterisk), Z_i from in-situ relative humidity gradient method (blue asterisk), purple, green and orange crosses same as described in (a); (c) wind speed (solid line) and wind direction (dotted line) from radiosonde (black) and UHF RWP (red); (d) air refractive index structure coefficient from UHF RWP with raw data (grey line) and filtered data as described in Sect. 3.2.2 (red line); (e) vertical velocity variance from UHF RWP with same colour code as (d); (f) TKE dissipation rate from UHF RWP with same colour code as (d); (g) NP0 (purple line) and NP3 (green line); (h) to (n) same as (a) to (g) respectively on 15 March 2018, at 14:15 UTC. Figure 6 (panels a to e) gives another example of UHF RWP measurements on 15 March 2018, this time with a marked external forcing, identified by a cloudy sky and by a high wind speed in the upper layer.

P2OA UHF RWP observations for 15 March 2018 at P2OA-CRA with the same description as Fig. 4 and cloud base height measured by CT25k ceilometer (black points). Figure ?? (panels h to n) confronts in-situ measurements of thermodynamical variables with the UHF RWP variables at 14:15 UTC that same day. In this case, the reflectivity maximum (at ~ 2500 m a. g. l.) does not correspond to Z_i (see Fig. ??k) which is assumed to be around 1500 m a. g. l. where the potential temperature gradient (Fig. ??h) becomes positive (stable layer) while the maximum of C_n^2 actually corresponds to the cloud base (see the black points in Fig. 6). However, the local minima of σ_w^2 and ε are well associated with Z_i (Fig. ??l and ??m).

Moreover, we can see between 15:00 UTC and 17:00 UTC in Fig. 6c the presence of virga (verified by observations of the weather radars of Météo-France). With droplet size close to the RWP wavelength, this induces a strong reflectivity (and C_n^2) on the entire profiles.

3 The CALOTRITON algorithm

3.1 Specific CALOTRITON specific objectives

In order to obtain reliable The new Z_i estimates with UHF RWP and to allow long time series analysis of the P2OA-CRA dataset, a Z_i -retrieval algorithm (CALOTRITON) was developed with 5 main objectives and constraints:

1. To restrict Z_i estimate to the convective boundary layer, by only considering daytime conditions and excluding precipitation periods.
2. To respect temporal continuity of Z_i growth and to follow it as finely as possible in time, in order to describe the smallest convective scales (5 to 30 minutes, Stull, 1988). Z_i should start close to the ground early in the day.
3. To manage complex cases: as in the presence of clouds (as shown as Fig. 6), or thermal internal boundary layer (TIBL), when cold air advection in the lower layers can create a new convective boundary layer e. g., in case of slope wind (Kossmann et al., 1998) or sea breeze (Durand et al., 1989).
4. To take into account abrupt CBL growth, which occurs in the presence of a residual neutral layer above Z_i , when the current CBL potential temperature gets to reach the residual neutral layer potential temperature (Blay-Carreras et al., 2014).
5. To use limited instrumental synergy in order to apply it in other sites (or measurement campaigns) equipped with a UHF RWP, and not to depend on the availability of an advanced instrument suite to establish Z_i estimate.

3.2 CALOTRITON operation

Figure 2 presents a scheme of CALOTRITON algorithm which is described in [details below, this section, and Table 3](#) [recapitulates the variables used at the different steps of CALOTRITON, with the corresponding time scale.](#)

Table 3. [Variables used in CALOTRITON, at the different steps of the algorithm, and their time interval](#)

Input variables	$C_n^2, \sigma_w, \varepsilon$ and w	2 min	Main input variables
	H	30 min	t_{init} assessment (optional)
	RH	1 s	Fog occurrence estimation (optional)
Filtered variables	$C_n^2, \sigma_w, \varepsilon$	5 min	
Calculated variables	NP_x, Z_i, ε	5 min	Key intermediate variables
	t_{init}	1 day	Key CBL growth starting variables
Auxiliary variable	CBH	1 min	Configuration optimization
Final variables	$Z_{iNP3std}$	5 min	Best estimate
	$Z_{iNP0std}, Z_{iNP0sup}, Z_{iNP0sub}$	5 min	Complementary estimates
	QF	5 min	Quality assessment

3.2.1 Restriction to CBL conditions

First, we consider UHF RWP data only above 225 m a. g. l. [This, and below 3000 m a. g. l., 225 m](#) is the first gate where data [are is](#) always of high quality. Only daytime data are selected to estimate Z_i from the UHF RWP. For this, sunrise and sunset times are retrieved as a function of date, altitude, latitude and longitude.

Precipitation periods (including virga) are excluded by a function based on empirical thresholds on C_n^2 and Doppler vertical velocity (w). Any profile which meets $C_n^2 > 10^{-14} \text{ m}^{-2/3}$ and $w < -1 \text{ m s}^{-1}$ over five consecutive levels is removed, as well

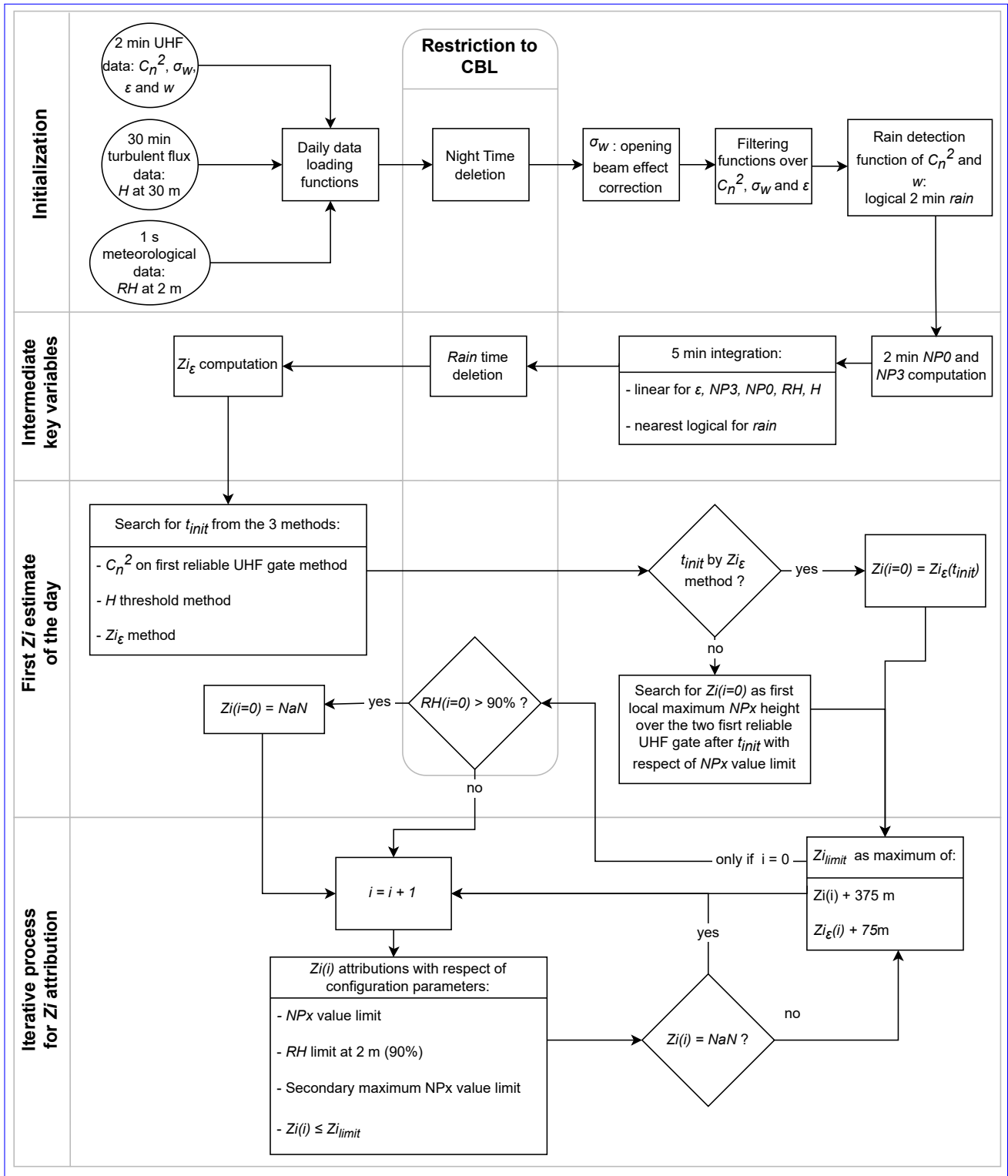


Figure 2. CALOTRITON organisation chart.

as all profiles occurring 15 minutes before and after (see Fig. 6c between 16:00 UTC and 17:00 UTC). We do not assign Z_i in case of fogs, notably due to the limitation of the UHF RWP below 225 m a. g. l.. It was found at P2OA site that relative humidity at 2 m larger than 90 % was associated to fog occurrence as confirmed by ceilometer measurements (not shown). We therefore take this as criterium for fog occurrence, and remove corresponding periods from the further analysis.

3.2.2 Definition of intermediate key variables Data averaging

As the reflectivity maximum does not always correspond to Z_i , especially in the case of a cloudy sky, we suggest using a new dimensionless variable which takes into account both, the increase of reflectivity at the sommital inversion and the decrease of turbulence: NPx (eq. 1) weights C_n^2 by σ_w power x , and allows for a better account of a large value of C_n^2 associated with a small value of σ_w . Dimensionless NPx is obtained by averaging values of C_n^2 and σ_w^x in the vertical for each profile (overlines in eq. 1):

$$NPx = \frac{C_n^2 / \overline{(C_n^2)}}{\sigma_w^x / \overline{\sigma_w^x}}$$

The choice of x is discussed in the Sect. 3.3.2. As examples, Figures 4f and 6f show cross sections of $NP3$ for the examples discussed previously.

In order to disregard non-meteorological disturbances (e. g., birds) on the UHF RWP signal, C_n^2 , σ_w and ε data are filtered by complementary sliding median filters:

- C_n^2 and ε : median over 6 minutes (3 points), none over height in order to keep the original UHF RWP vertical resolution of 75 m (dz).
- σ_w : median over 8 minutes (4 points), and a median over 225 m (3 points), because of a more pronounced spatio-temporal variability of these data (see Fig. 4d, 6d 8d). We use coarser filters for σ_w to compensate for the fact that C_n^2 and ε are already integrated over the 5 beams.

If a larger integrated time is chosen, the corresponding median time filter should be adjusted and applied to C_n^2 , ε and σ_w .

3.2.3 Definition of intermediate key variables

As the reflectivity maximum does not always correspond to Z_i , especially in the case of a cloudy sky, we suggest using a new dimensionless variable which takes into account both, the increase of reflectivity at the sommital inversion and the decrease of turbulence: NPx is computed with these filtered data (eq. 1) weights C_n^2 by σ_w power x , and allows for a better account of a large value of C_n^2 associated with a small value of σ_w . Dimensionless NPx is obtained by averaging values of C_n^2 and σ_w^x up to 3000 m for each profile (overlines in eq. 1):

$$265 \quad NPx = \frac{C_n^2 / (\overline{C_n^2})}{\sigma_w^x / \overline{\sigma_w^x}} \quad (1)$$

NPx is computed with the filtered data discussed previously (section 3.2.2) and is linearly integrated over a 5 minute time step to describe the smallest characteristic convective scale. If a larger integrated time is chosen, the corresponding median time filter should be adjusted and applied to C_n^2 , ϵ and σ_w . The choice of x is discussed in the Sect. 3.3.2. As examples, Figures 4f and 6f discussed later, show cross sections of $NP3$ in a simple and complex case respectively. Note that this approach is based on the same main assumption as in the methods proposed by Heo et al. (2003) and Bianco and Wilczak (2002), who also combined the need of an increased reflectivity and a decrease of turbulence.

We also consider another variable, purely defined by the level of turbulence: Z_{i_ϵ} is the height above the surface at which the TKE dissipation rate ϵ falls below $5 \times 10^{-4} \text{ m}^2 \text{ s}^{-3}$. This technique was previously used by (Couvreur et al., 2016; Nilsson et al., 2016a). It thus represents a rough estimate of the depth of significant turbulence. Z_{i_ϵ} is computed on filtered and integrated ϵ data (5 minutes as NPx). In order to consider only the Z_{i_ϵ} that would respect a certain temporal continuity, a sliding median filter over 15 minutes (3 points) is applied on Z_{i_ϵ} .

NPx is the core variable of CALOTRITON, but Z_{i_ϵ} will help us on documenting the associated turbulence, and optimize the selection of the most appropriate local maximum of NPx as an estimate of Z_i (we hereafter call this selection " Z_i attribution").

280 3.2.4 Determination of the first Z_i estimate of the day

In a typical CBL development, Z_i starts close to the ground, below the UHF RWP detection limits (225 m), and grows until it reaches a plateau in the early afternoon (Stull, 1988). It is therefore necessary to wait for some time (called t_{init}) before Z_i can be detected by the UHF RWP. We found that the sensible heat flux, which governs the evolution of Z_i , remains very low (less than a few tens of W) at least until an hour and a half after sunrise (not shown). Therefore, t_{init} is not defined before 1.5 hour after sunrise.

Several methods are used to determine t_{init} . The first is based on C_n^2 at the first reliable UHF RWP gate (225 m a. g. l.) and considers t_{init} as the time when the 30-minute sliding median exceeds its daily mean value. That way, it is investigated when an increase in C_n^2 becomes significant and may correspond to Z_i . The second method is based on the measured sensible heat flux (H) and considers t_{init} when H exceeds a significant threshold of 50 W m^{-2} . t_{init} is taken as the earliest time over those two. The first assigned Z_i of the day ($Z_i(i=0)$) can only be established at a local maximum of the vertical profile of NPx located at one of the two first reliable levels of the UHF RWP and occurring after t_{init} .

Sometimes, a thin layer is mixed by dynamical turbulence before sunrise, e.g., in the presence of a low level jet. In order to take those situations into account, we allow the attribution of the first Z_i at the height of Z_{i_ϵ} if the latter corresponds exactly to the height of the NPx maximum of the profile, independently of t_{init} , and provided that this attribution is always done 1.5 hour after sunrise.

This initialization process is somehow similar to Molod et al. (2015), who called this time the ‘emergence time’, and determined it based on the same principle, i. e. they also consider a first good confidence gate and look for the first determinable Z_i at this level, but in a different way.

3.2.5 Iterative process for Z_i attribution

300 Once the initial Z_i is found, the search for subsequent Z_i is done by temporal iteration on the most significant local maximum of NPx that is located within a vertical growth limit of 375 m since its last effective attribution. Residual layers or clouds above Z_i can potentially return a higher signal contribution to NPx than Z_i itself, and might be misinterpreted if located within the 375 m growth limit. To take this into account, the algorithm allows attributions on local secondary maxima of NPx below the first if the value of the corresponding NPx is at least 90 % of the first maximum value of NPx before 10:00 UTC
305 and 50 % after. These empirical values are discussed in section 3.3.2 and named relative thresholds of secondary maximum of NPx . Finally, a minimal value of NPx is required for attribution and fixed to the mean profile value of NPx in order to take into account a certain significance.

Sometimes, strong growth of Z_i can occur and exceed the imposed limit (375 m). This motivated us to use Z_{i_ε} , in order to consider up to which level significant turbulence is found. If at i time, $Z_{i_\varepsilon}(i)$ is higher than the last effective attribution plus
310 the growth limit, then $Z_i(i)$ can be searched up to $Z_{i_\varepsilon}(i) + dz$ (where $dz = 75$ m).

3.3 Algorithm parameter choice

3.3.1 Parameter optimization

All the parameters presented above were obtained empirically by subjectively judging the quality of the attributions of Z_i for about 100 days in 2018 at P2OA-CRA. In order to verify their quality in a more objective way and possibly to adjust some
315 parameters, we compared the estimates of Z_i with the lowest cloud base height (CBH) measured by the CT25k ceilometer within a 5-minute interval around each attribution. This comparison is based on data from December 2016 to December 2019. When comparing two configurations with the distributions shown in Fig. 3, one would favour the configuration which leads to less attributions above cloud base and lower values of ε at Z_i .

Figure 3 shows an example of the results of this comparison, for Z_i estimates based on either $NP3$ or $NP0$, with the use
320 of the optimal parameters listed in Table 4. Figure 3a shows the distribution of the set of Z_i attributions for the different NPx ($x=0$ and $x=3$), and indicates more attributions by $NP3$, especially for $Z_i < 700$ m. Figure 3b shows the distribution of the differences between Z_i and CBH.

It can be seen that there are slightly more attributions above the cloud base when using $NP0$. Figure 3c presents the distribution of all ε values at Z_i height, and shows that $NP3$ attributions tend to get lower ε values at Z_i height. The fact
325 that $NP3$ attributions of Z_i are more often lower than $NP0$ attributions and associated with lower ε values is a sign of better quality attributions.

When clouds are present, the difference amount-between Z_i estimates with $NP3$ and $NP0$ is on average twice as large as in clear sky cases, due to the complexity of the atmosphere in cloudy conditions. Thus, the observed differences between Z_i attributions with $NP3$ and $NP0$ give an indication of the CBL complexity.

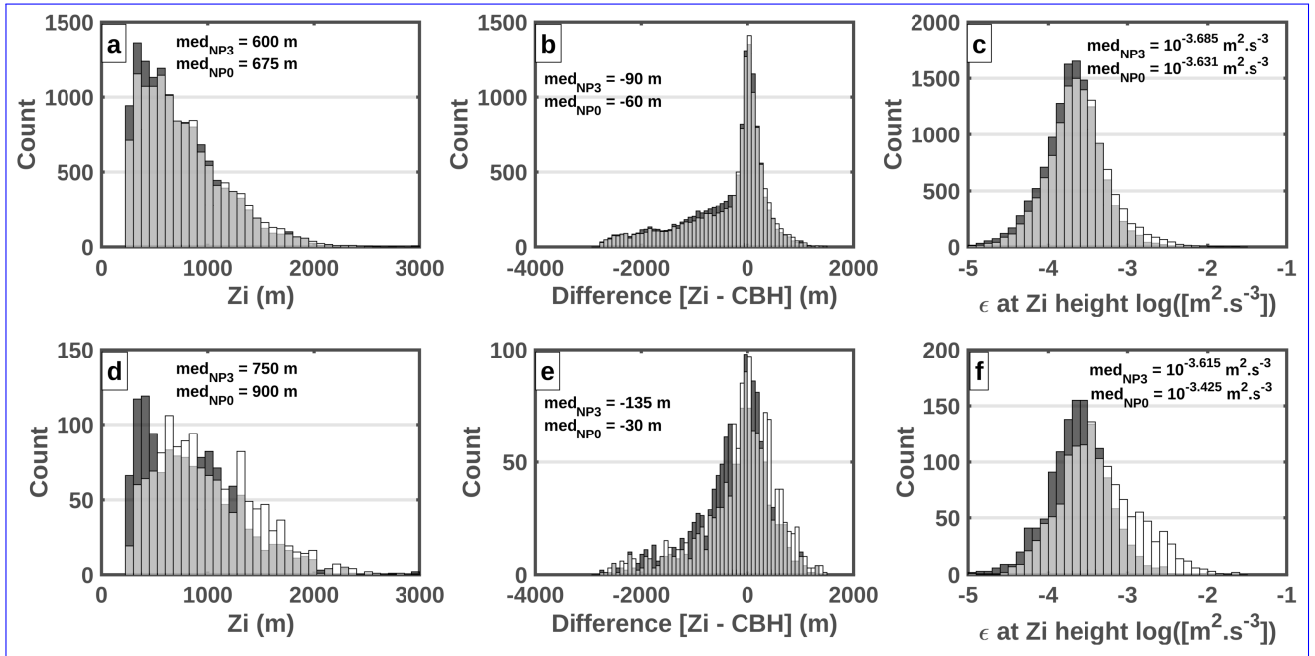


Figure 3. Histograms showing the differences between the distributions of $Z_{iNP0std}$ (white bar) and $Z_{iNP3std}$ (black bar) in presence of cloud measured by the CT25k ceilometer from december 2016 to december 2019: (a) Z_i distribution, (b) distribution of difference between Z_i and cloud base height; (c) ϵ value distribution at Z_i height. (d) to (f) are respectively the same as (a) to (c) but considering only attributions which present more than 225 m difference between $Z_{iNP0std}$ and $Z_{iNP3std}$. For each distribution, the median values are indicated by med_{NP3} and med_{NP0} , for distribution from $Z_{iNP3std}$ and $Z_{iNP0std}$ respectively.

Table 4. List of best parameters for CALOTRITON configuration

Parameter	Value	Comments
Integration time	5 minutes	
Time median filter C_n^2	3 points	~ 6 minutes
Time median filter ϵ	3 points	~ 6 minutes
Time median filter σ_w	4 points	~ 8 minutes
Height median filter C_n^2	0 points	0 m
Height median filter ϵ	0 points	0 m
Height median filter σ_w	3 points	225 m
Growth limit	375 m	between two effective assignments
Relative humidity limit at 2m	90 %	
NPx Value limits	NPx profile mean	
Secondary maximum NPx value limit	90% before and 50% after 10:00 UTC	And respect NPx Value limit
$Z_{i\epsilon}$ option	True	To exceed the growth limit

330 Figure 3d to 3f presents the same figure as the top panel (Fig. 3a to 3c) but only considering the attributions by $NP3$ and $NP0$ when they differ for more than 225 m from each other. This represents only 10 % of the total attributions. The same conclusions as previously stated can be drawn, even more clearly here. We therefore confirm that $NP3$ statistically gives better results.

3.3.2 Tested parameters and optimum set

335 In this way, the set of NPx for $x = 1$ to 5 were compared two by two with the configuration presented in Table 4. It was noted that attributions were potentially better for $x = 3$ rather than $x = 0, 1$ or 2. However, no significant trend was noticed for $x \geq 3$. We limit us to $x = 3$ in order to keep attributions more predominantly based on C_n^2 ~~than σ_w~~ .

340 In this section, only a few results of our search for the best parameters by attribution distribution analysis are presented. All are based on $NP3$. The largest differences appeared between whether or not we consider the a limit on relative humidity. Not setting a limit allows about 4% more attributions in clear sky and 40% more in the presence of clouds. Among those 40%, half of them corresponds to cloud base heights below 225 m, which is the first level of the UHF RWP. Considering the limit on relative humidity, 13% of all attributions in the presence of clouds take place 225 m above the cloud base, compared to 22% without a limit. This limit therefore both avoids attributions in the presence of clouds whose base is below the UHF RWP lower limit and reduces the number of attributions above the cloud base by half.

345 The methods for the search of t_{init} were tested. Using solely the C_n^2 maximum technique leads to almost no difference in Z_i attributions, but using additionally additionally using the technique based on sensible heat flux leads to 3% more attributions.

Other values related to the growth limit were also tested. It was noticed that a limit of 300 m with the last effective attribution potentially allows to obtain better quality attributions but leads to a reduction of 3% of the attributions compared to a limit of 375 m. Empirically, it was found that 300 m was not sufficient to properly track the evolution of Z_i compared to 375 m. On the other hand, a 450 m growth threshold dit did not improve statistically the results. Although it leads to an increase of the total number of attributions by 3%, all additional attributions under cloudy skies were above cloud base. This is the reason we finally chose 375 m as the optimal growth threshold.

Other important parameters are the values selected for the relative thresholds of secondary maximum NPx on which attributions are possible. Not setting a limit leads to an increase of 40% in attributions above $CBH + 225$ m, associated with higher ε values, which is thus less appropriate. Thresholds of 50% and 90% were tested over the whole day and it was found that 50% led to more attributions over residual layers than 90%, especially in the morning. In contrary, a threshold of 90% leads to more attributions inside the CBL, especially in the afternoon. This is why a threshold of 90% before 10:00 UTC and 50% afterwards was chosen. A threshold of 75% for the whole day was also tested but provided poorer results.

3.3.3 Final assignment and flags

360 As we have seen previously, the difference between $NP0$ and $NP3$ attributions with the parameter set as described in Table 4, gives a useful and complementary information about the complexity of the lower troposphere. This is why we perform four estimates of Z_i :

- $Zi_{NP3_{std}}$: estimated with standard configuration for $NP3$ as described in Table 4, considered as the best attributions.
- $Zi_{NP0_{std}}$: estimated with standard configuration for $NP0$ as described in Table 4
- 365 – $Zi_{NP0_{sup}}$: estimated for $NP0$ as described in Table 4, but without the relative humidity limit at 2m-2m and NPx value limit, no possibility to take into account a secondary maximum of NPx , no t_{init} restriction (only after sunrise), and 375 m growth limit between the searched Zi and the maximum Zi already ~~allocated~~allocated with this configuration. This configuration allows to search for levels higher than the estimates made with a standard configuration, which could correspond to Zi if the standard configurations assign on a TIBL top or could correspond to the top of a residual layer.
- 370 – $Zi_{NP3_{sub}}$: estimated for $NP3$ as described in Table 4, but without limit on secondary NPx maximum and NPx limit value which considers only the median profile. This configuration allows us to search for levels lower than the estimates made with a standard configuration, which could correspond to a TIBL top, or expected Zi if standard configurations assign on a residual layer top.

Our best proposed estimate is $Zi_{NP3_{std}}$, for the reasons explained before. But the four estimates embed the large complexity
375 that is often observed in the lower troposphere.

In order to qualify this complexity and to facilitate the correct use of the four estimates, a quality flag QF is defined :

- flag-QF = 1: all attributions are equal. It indicates a very good confidence in the assignment quality and a textbook case.
- flag-QF = 2: only $Zi_{NP3_{std}}$, $Zi_{NP0_{std}}$ and $Zi_{NP3_{sub}}$ are equal. It indicates a good confidence in the assignment quality and the likely presence of a residual layer above Zi , which it would be located at $Zi_{NP0_{sup}}$. It also indicates that the Zi
380 estimate does not match with the height of the C_n^2 maximum.
- flag-QF = 3: only $Zi_{NP3_{std}}$, $Zi_{NP0_{std}}$ and $Zi_{NP0_{sup}}$ are equal. It indicates a medium confidence in the assignment quality and the likely presence of a TIBL located at $Zi_{NP3_{sub}}$.
- flag-QF = 4: only $Zi_{NP3_{std}}$, $Zi_{NP0_{std}}$ are in exact agreement. It indicates a medium confidence in the assignment quality and the likely presence of both a TIBL and a residual layer, located at $Zi_{NP3_{sub}}$ and $Zi_{NP0_{sup}}$, respectively.
- 385 – flag-QF = 5: no agreement between the four attributions of heights. This indicates poor confidence in the assignment quality, and a highly complex case.

Others flags could be produced, in order to more thoroughly document the meaning of those various estimates. They could for example qualify the temporal continuity of $Zi_{NP3_{std}}$ (occurrence of abrupt changes,...) or the consistency of $Zi_{NP3_{std}}$ with Zi_ϵ .

390 4 Illustrating case studies

4.1 **Example case studies**

All the assignments made by the four sets-

In this section, we present three study cases to illustrate the capability of CALOTRITON, and the improvements of Z_i estimates are shown in the retrieval relatively to a more standard approach:

- 395
- A reference simple clear sky case (27 October 2021, at P2OA)
 - A complex cloudy sky case (15 March 2018, at P2OA)
 - A complex multiple layering clear case (27 July 2021, during the LIAISE field experiment)

4.1 Clear sky case at P2OA

Figure 4 shows the height-time section of four UHF-based variables defined before: the air refractive index structure coefficient C_n^2 (Fig. 4-a), the air vertical velocity variance σ_w^2 (Fig. 6 and 4b), the turbulent kinetic energy (TKE) dissipation rate ε (Fig. 4c), and the new combined parameter $NP3$ (Fig. 8-

400

4.1.1 Clear-sky case

We note the very high 4d).

The downward short-wave radiation (white line) and the sensible heat flux (blue line) are overlaid on all panels. The short-wave radiation shows that this day was mainly clear, with only a few thin and occasional cirrus clouds in the afternoon. Sensible heat flux shows a typical diurnal cycle. Also overlaid are different estimates of Z_i , defined in the previous section: $Z_{i_{NP0_{std}}}$, $Z_{i_{NP0_{sup}}}$, $Z_{i_{NP3_{std}}}$, $Z_{i_{NP3_{uh}}}$ and the intermediate variable Z_{i_ε} . We note for this case a very large consistency between the four different estimates in the clear-sky case shown in Fig. 4. Therefore, $Z_{i_{NP3_{std}}}$ has a good confidence index, except around 15:30 UTC, where $Z_{i_{NP0_{std}}}$ is slightly lower than $Z_{i_{NP3_{std}}}$. Figure ?? shows data from a radiosonde launched $Z_{i_{NPx}}$. That means whatever the method, standard or more sophisticated, taking account on turbulence intensity or not, they all agree for Z_i estimation for the CBL growth, and simply match to the absolute maximum reflectivity for most of the time.

405

410

In order to make the correspondence between the UHF RWP and the thermodynamical profiles, Fig. 5 compares in-situ measurements of thermodynamical variables measured by radiosondes with the UHF RWP measured variables at 13:35 UTC the same day at CRA. In, on this same clear day of 27 October 2021. The comparison shows that the absolute maximum reflectivity corresponds well to the CBL top, characterized by a strong gradient of potential temperature and mixing ratio (Fig. 5a and 5b). It also shows that σ_w^2 (Fig. 5e) and ε (Fig. 5f) are small at this height, leading to a local minimum. In "ideal" clear days, without external forcing, we would typically not observe significant turbulence above Z_i (Fig. 1e). In this case, forcing is small, with weak wind but the wind shears still generates significant turbulence (Fig. 4c). In a subjective way, we estimate Z_i at about 550 m from this radiosonde, where a strong potential temperature gradient is observed, associated with a strong humidity gradient (mixing ratio and relative humidity). This height is in good agreement with all the estimates made by CALOTRITON -This is at that time, and with the simplest standard estimate of Z_i from RWP. This case is thus a textbook example of a typical clear sky case (see the nearly undisturbed diurnal course of the incoming shortwave radiation in, with $QF = 1$ for most of the

415

420

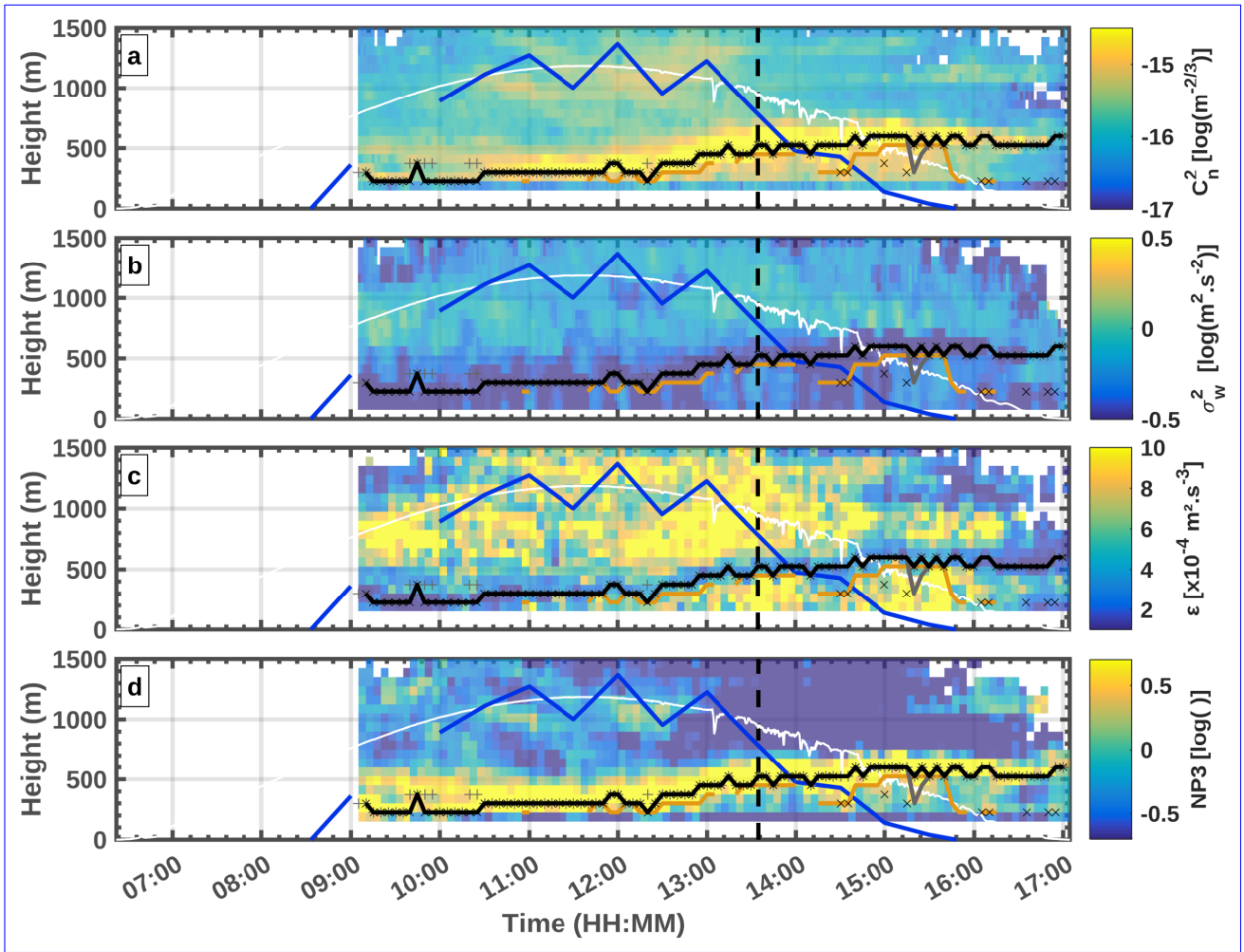


Figure 4. UHF RWP observations for 27 October 2021 at P2OA-CRA during clear sky: (a) filtered C_n^2 in log scale, (b) filtered σ_w^2 in log scale, (c) filtered and integrated ε in log scale, (d) integrated NP3 in log scale. For all panels, Z_i estimates as described in Sect. 3.2.2 and 3.3.3: Z_{i_ε} (orange line), $Z_{i_{NP3_{std}}}$ (gray line), $Z_{i_{NP3_{sup}}}$ (gray crosses +), $Z_{i_{NP3_{std}}}$ (black line), $Z_{i_{NP3_{sub}}}$ (black crosses x); and based on the same ordinate axis (but with different units): short wave down ($W m^{-2}$) (white line), sensible heat flux ($deciW m^{-2}$) (thick blue line). The vertical dashed line correspond to the time of the discussed radiosounding.

425 day (Fig. 4), with flag = 1 for most of the day. $Z_{i_{NP3_{std}}}$ has consequently a good confidence index, except around 15:30 UTC, where $Z_{i_{NP3_{std}}}$ is slightly lower than $Z_{i_{NP3_{std}}}$. Note on Fig. 4 that Z_{i_ε} remains equal or below those estimates, and especially decreases in late afternoon, with a strong decay of the surface flux. This is one typical late afternoon transition scenario, as described in Grimsdell et al. (2002) and Lothon et al. (2014). $Z_{i_{NP3_{sub}}}$ also interestingly decays during the same phase, thus defining a potential pre-residual layer, situated between $Z_{i_{NP3_{sub}}}$ (or Z_{i_ε}) and $Z_{i_{NP3_{sup}}}$ (or $Z_{i_{NP3_{std}}}$). The pre-residual layer is defined when the surface heat flux is not strong enough anymore to keep the mixing up to the midday somital inversion, and falls between the thinning turbulence layer and the residual inversion (Nilsson et al., 2016b; Lothon et al., 2023). The different

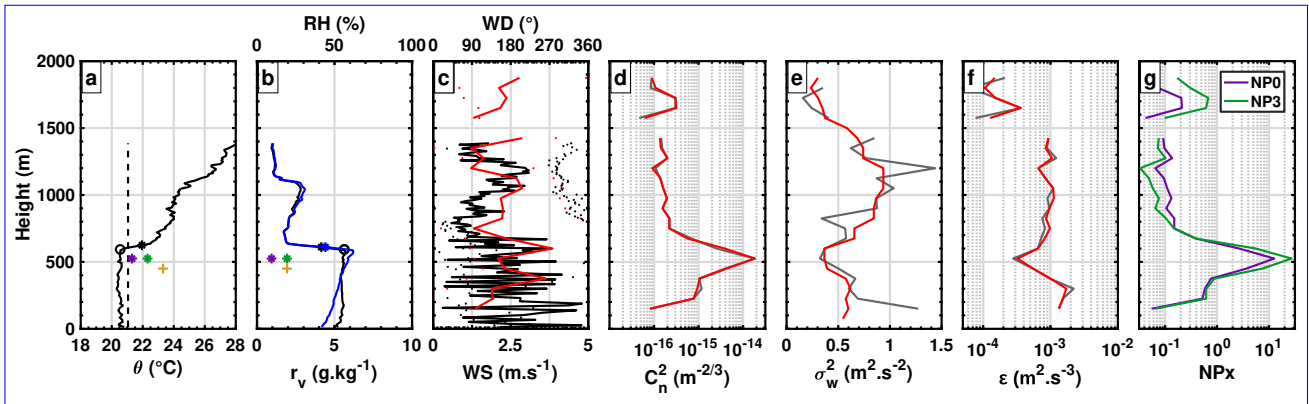


Figure 5. Profiles measured by radiosondes and UHF RWP at P2OA-CRA, on 27 October 2021, at 13:35 UTC: (a) potential temperature (black solid line), surface potential temperature + 0.25°C (black dashed line), Z_i from in-situ subjective method (black circle), Z_i from in-situ potential temperature gradient method (black asterisk), $Z_{i_{NP0_{std}}}$ (purple 'x'), $Z_{i_{NP0_{sup}}}$ (purple '+'), $Z_{i_{NP3_{std}}}$ (green 'x'), $Z_{i_{NP3_{sub}}}$ (green '+'), $Z_{i_{\epsilon}}$ (orange '+'); (b) mixing ratio (black line) and relative humidity (blue line), Z_i from in-situ mixing ratio gradient method (black asterisk), Z_i from in-situ relative humidity gradient method (blue asterisk), purple, green and orange crosses same as described in (a); (c) wind speed (solid line) and wind direction (dotted line) from radiosonde (black) and UHF RWP (red); (d) air refractive index structure coefficient from UHF RWP with raw data (grey line) and filtered data as described in Sect. 3.2.2 (red line); (e) vertical velocity variance from UHF RWP with same colour code as (d); (f) TKE dissipation rate from UHF RWP with same colour code as (d); (g) NP0 (purple line) and NP3 (green line).

430 estimates made in CALOTRITON thus can help identify interfaces and layers, in the complex afternoon transition phase. Standard and simple methods do not enable to describe this subtle and still poorly understood complexity.

4.1.1 Cloudy complex case

For the more complex cases shown in Fig. 6, the four different Z_i estimates

4.2 Cloudy complex case at P2OA

435 Figure 6 gives another example of UHF RWP measurements on 15 March 2018, this time with a marked external forcing, identified by a cloudy sky and by a high wind speed in the upper layer. For this figure, the cloud base height measured with the ceilometer is added, also revealed by the downward short-wave radiation. In this complex case, the maximum of C_n^2 remains most of the day between 2000 m and 3000 m, related with the clouds and associated hydrometeors, rather than to the top of the CBL. This makes $Z_{i_{NP0_{sup}}}$ high in this nearby cloud layer. Between 10:00 UTC and 11:30 UTC, this maximum of C_n^2 is competitive with the local maximum below, which is what we can interpret as the top of the growing CBL, and which is better detected with NP3. Between 16:00 UTC and 17:20 UTC, the reflectivity field shows the presence of virga (verified by observations of the weather radars of Météo-France). Where droplet size is close to the RWP wavelength, this induces a strong reflectivity (and C_n^2) on the entire profiles. For this more complex case, $Z_{i_{NP0_{std}}}$, $Z_{i_{NP3_{std}}}$ and $Z_{i_{NP3_{sub}}}$ are consistent only until 11:00 UTC. After this time, $Z_{i_{NP0_{std}}}$ and $Z_{i_{NP0_{sup}}}$ are higher than $Z_{i_{NP3_{std}}}$ and $Z_{i_{NP3_{sub}}}$, suggesting that the latter

445 latter may be assigned on the top of a TIBL. After 11:30 UTC, the assignments based on NP3 become more discontinuous

due to the limit of NPx values (NPx profile mean). This discontinuity indicates an increased uncertainty in the attributions. $Zi_{NP0_{sup}}$ is then systematically located above the others, suggesting that $Zi_{NP3_{std}}$ may potentially identify the top of a TIBL. However, we believe that these attributions are correct, as they are located at the height where the strongest wind shear is observed.

450 ~~Between 14:00 UTC and After 15:00 UTC we find more continuous attributions of $Zi_{NP3_{std}}$. Data from a radiosonde taken~~
~~Fig. 6 shows more discontinuity on $Zi_{NP3_{std}}$ attributions, demonstrating a CBL complexity with small incoming shortwave radiation, no positive sensible heat flux and the occurrence of precipitation mentioned above.~~

In order to better interpret this complex day, Figure 7 compares in situ measurements of thermodynamical variables with the UHF RWP variables at 14:15 UTC are shown in Fig. ??h to ??n. UTC that same day. In a subjective way, Zi can be

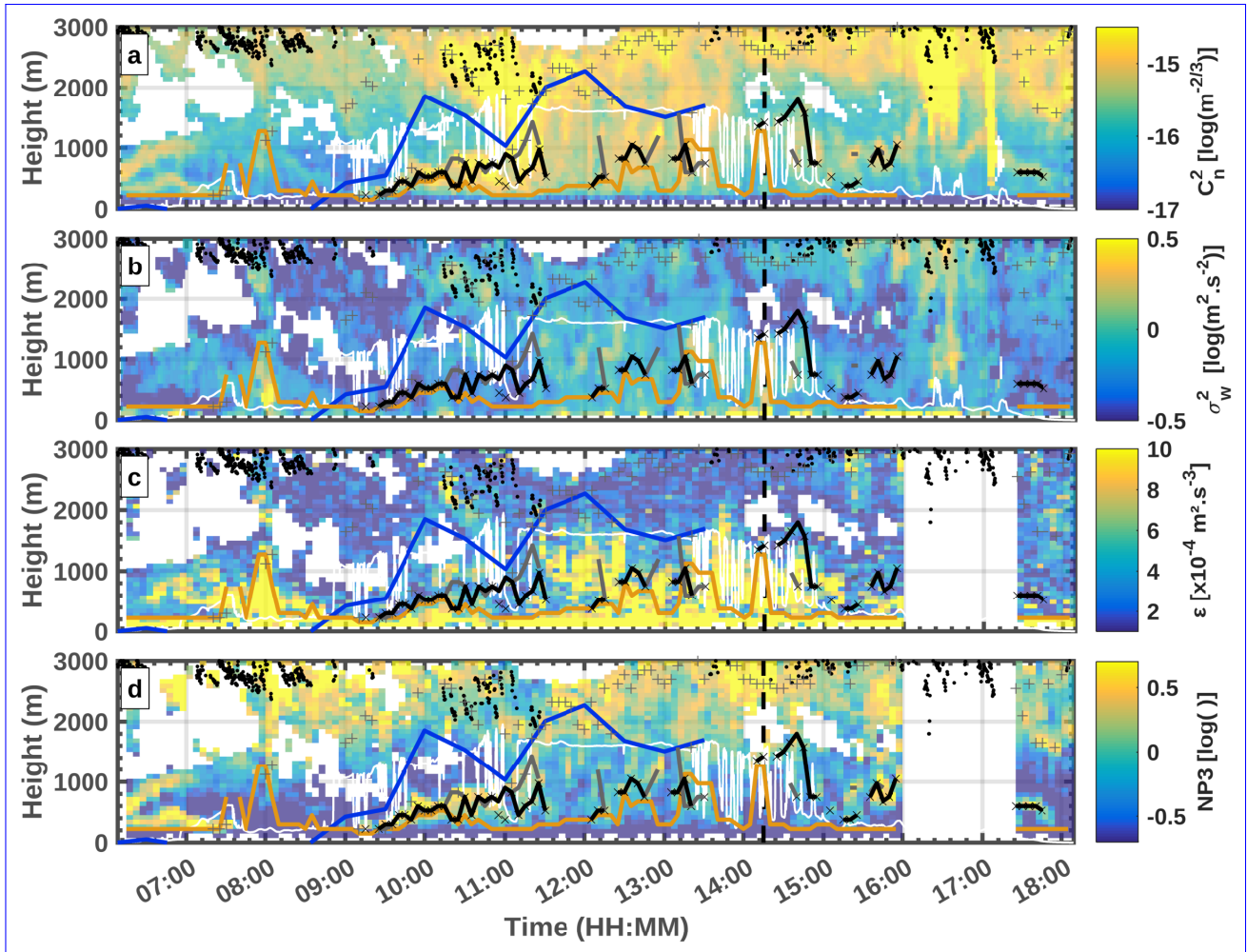


Figure 6. LAERO UHF RWP observations for 15 March 2018 at P2OA-CRA with the same description as Fig. 4 and cloud base height measured by CT25k ceilometer (black dots).

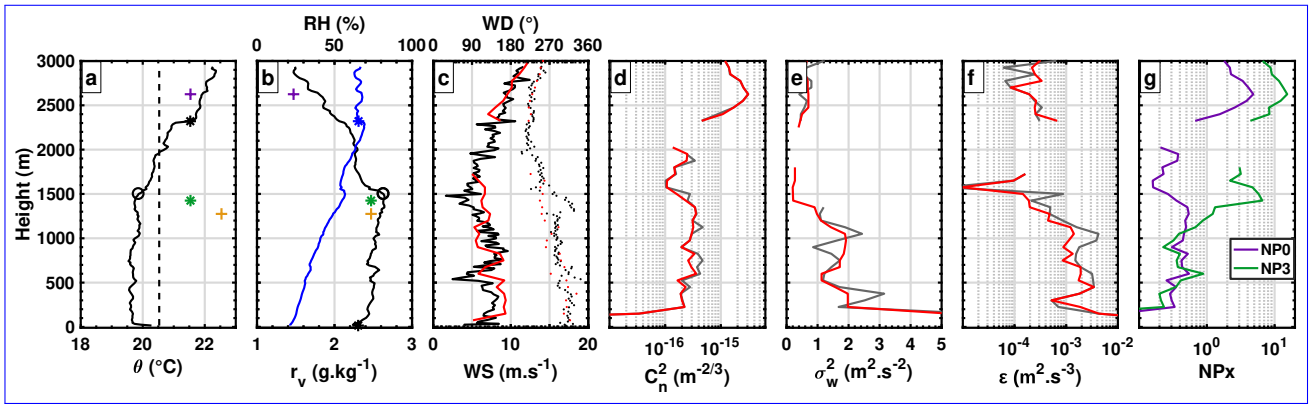


Figure 7. Same as Fig. 5 for 15 March 2018, at 14:15 UTC.

455 estimated at 1500 m from this radiosounding (Fig. 7a), the height where the atmosphere starts to be stable (positive θ gradient), also associated with a strong discontinuity in the mixing ratio profile. This height corresponds well to $Zi_{NP3_{std}}$. ~~We also note that~~ Though the absolute maximum of C_n^2 (Fig. 7d) and also $Zi_{NP0_{sup}}$ seems to correspond to the top of a residual layer around 1500 (indicated in Fig. 7a) correspond to an inversion around 2500 m, identified by a strong potential temperature gradient. $Zi_{NP0_{std}}$ is not successful because of the limit on the NPx values. There is also This actually corresponds to a cloud
 460 base (see the black dots in Fig. 6) which is decoupled from the CBL. $Zi_{NP0_{std}}$ is thus unsuccessful here. There is no marked local maximum of C_n^2 at the height of Zi estimated from the in-situ radiosonde, while the but σ_w profile has (Fig. 7e) and ϵ (Fig. 7f) profiles have a well marked local minimum, forming a marked local maximum on NP3.

~~After 15:00 UTC, Fig. 6 shows more discontinuity on $Zi_{NP3_{std}}$ attributions, demonstrating a CBL complexity with small incoming shortwave radiation, no positive sensible heat flux and rain precipitation characterized by high C_n^2 values.~~

465 This example illustrates the benefit of taking σ_w into account via NPx at-with $x > 0$ in the attribution of Zi . It also shows the advantage of the various Zi estimates to identify different interfaces in the case of complex vertical structure. Of course, the large complexity of this case and the weak CBL encountered in some phases of the day due to clouds and precipitation, makes is still difficult to deal with.

4.2.1 Clear sky with multiple layering

470 4.3 Clear sky with multiple layering during LIAISE

The use of the LIAISE dataset (Boone et al., 2021) allows us to test the CALOTRITON algorithm with the same UHF RWP at a different location and under different meteorological conditions. During the LIAISE campaign, the P2OA RWP was deployed from June 2021 to October 2021 in the semi arid region of Lleida, Spain, at a distance of about 15 km from large areas of irrigated crops.

475 ~~P2OA UHF RWP observations for 27 July 2021 at Els Plan (Spain) during the LIAISE campaign with the same description as Fig. 4, and in addition, Zi from in-situ radiosounding estimation: from parcel method (blue ‘+’), from potential temperature~~

gradient method (pink '+'), from relative humidity gradient method (orange '+'), from mixing ratio gradient method (green '+'), from subjective method (black '+').

480 Same as Fig. ??, but with profiles measured by radiosounding and P2OA-UHF RWP at Els Plan (Spain) during the LIAISE campaign on 27 July 2021, (a)-(g) at 11:00 UTC, and (g)-(n) at 18:00 UTC.

Figure 8 exemplifies illustrates the complexity that can be observed in clear sky conditions in this region, and proves tests the capability of CALOTRITON under CBL-multilayering conditions. for CBL with multilayer conditions. The analyses of this rich dataset have only recently started, but the study by Jimenez et al. (2021) already testimonies to this complexity.

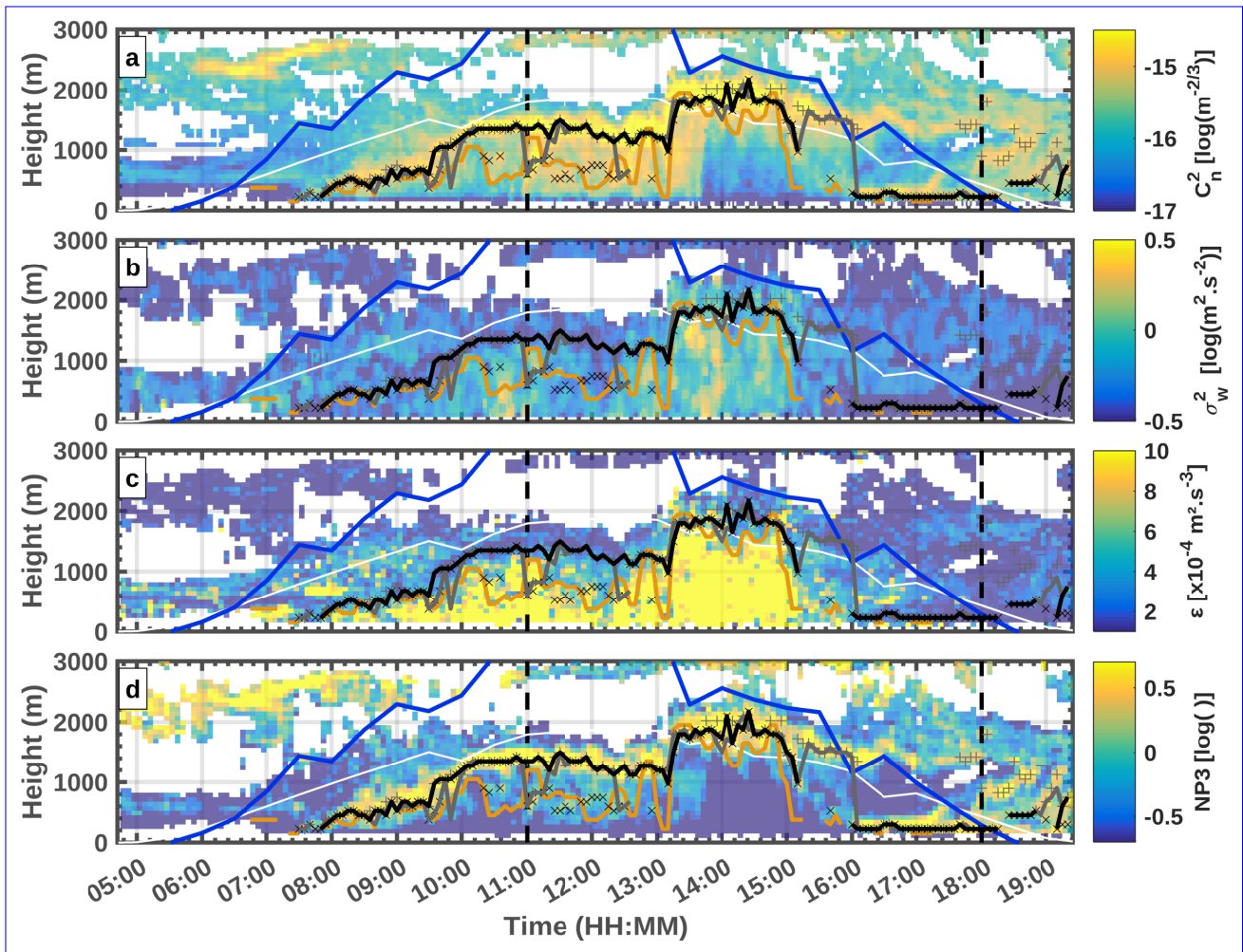


Figure 8. LAERO UHF RWP observations for 27 July 2021 at Els Plans (Spain) during the LIAISE campaign with the same description as Fig. 4.

485 Early in the morning, an elevated local (actually absolute) maximum of C_n^2 is present between 2 and 3 km. This corresponds to a high inversion, potentially coming from a residual transported layer (shown later). An algorithm purely based on maximum

C_n^2 would start the day with this erroneous Z_i estimate. In CALOTRITON, the process of finding the first estimate of the day at the first possible gate enables to avoid this situation. Most of the various Z_i estimates agree until 09:30 UTC. Between 10:00 UTC and 13:00 UTC, $Z_{i_{NP3_{sub}}}$ indicates the potential presence of a TIBL located below 1000 m. At 11:00 UTC, $Z_{i_{NP0_{std}}}$ is at the level of $Z_{i_{NP3_{sub}}}$ at about 600 m. ~~Figure ??~~ Firstly, note the maximum C_n^2 discussed previously is still present at 11:00 UTC on Fig. 8a, and corresponds to a large moisture and temperature inversion. It is not thin, but associated with a large change in the water vapour mixing ratio.

Figure 9 shows measurements from a radiosonde taken at this time. In the first 1500 m, we notice the presence of two

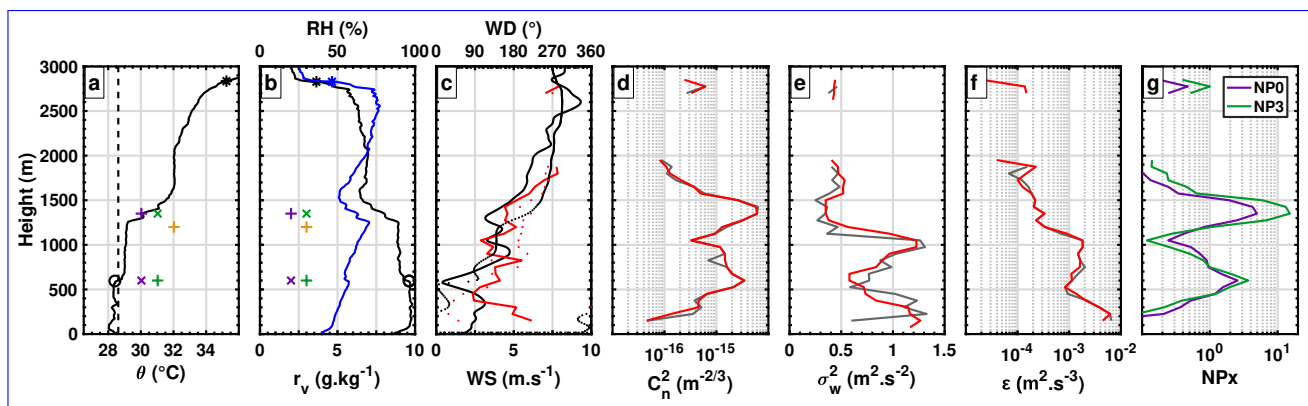


Figure 9. Same as Fig. 5, but with profiles measured by radiosounding and LAERO UHF RWP at Els Plans (Spain) during the LIAISE campaign on 27 July 2021 at 11:00 UTC

superimposed layers with constant potential temperatures and mixing ratio (Fig. ??a and ??9a and 9b), separated by a thermal inversion at 600 m. Strictly speaking, according to the definition of the thermodynamic approach, Z_i should be located at the top of the first layer, since the surface over-adiabaticity (28°C) theoretically does not allow a parcel of air to cross the inversion at 600 m (29°C above). By a scalar concentration approach, Z_i could also be attributed to 600 m where a discontinuity in the mixing ratio is indeed observed. The latter is, however, not considered very strong and the fact that a constant (but slightly different) mixing ratio is observed above and up to 1300 m, indicates that mixing seems to take place up to this height. The mixing may actually be horizontally homogeneous, with mixing within this upper layer. An earlier sounding, at 10:00 UTC (not shown here), reveals that the CBL was well mixed up to 1200 m a. g. l. this day over this dry site. What is seen at 11:00 UTC on Fig. 9a and 9b is an intrusion of a nearby boundary layer likely advected into the region from the north-east, that is from the irrigated site, which has much thinner CBL. The cooler and moister air observed over the dry site in Figure 8b up to 600 m is consistent with air coming from the irrigated area. In this case, over Els Plans, some turbulence structures may be able to overcome the 600 m high inversion, and some others not. We indeed find high turbulence values ($\epsilon > 5 \times 10^{-4} \text{ m}^2 \text{ s}^{-3}$) up to 600 m. Measurements from another instrumented site, located 30 km northwest in the irrigated area, indicate a boundary layer height of 200 m at this same time. Figure 8b shows that the cooler and moister air observed over the dry site, where the RWP is located, comes from the irrigated area. Confronting these radiosonde data with This turbulence contributes to mix both layers and erode the inversion. This is observed later in the soundings (not shown). Comparing the 11:00 UTC radiosonde profile

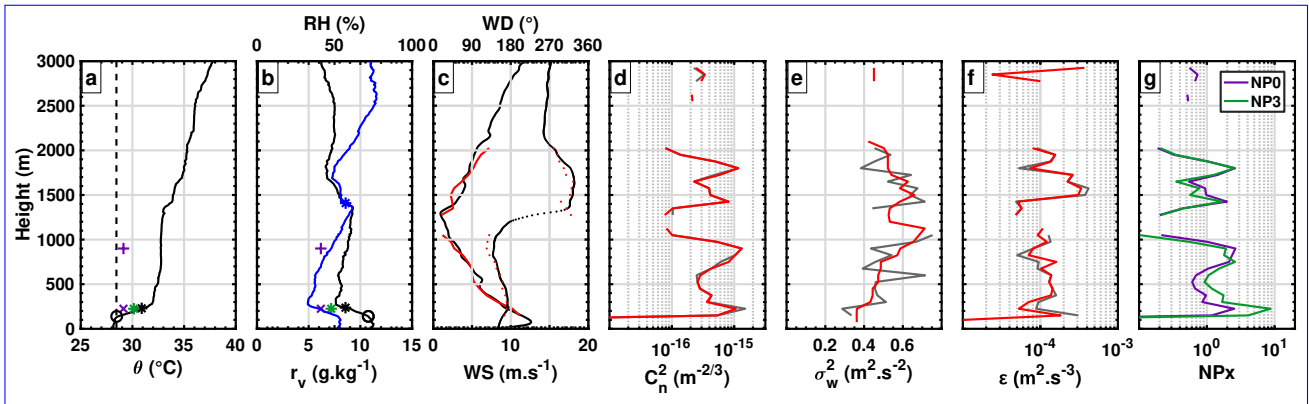


Figure 10. Same as Fig. 9 at 18:00 UTC.

the UHF RWP data, we suspect estimates, $Z_{i_{NP3_{std}}}$ defines Z_i at 1300 m, as $Z_{i_{NP3_{std}}}$, with the presence of a TIBL inside, whose top would be located at 600 m and detected by $Z_{i_{NP3_{sub}}}$ and $Z_{i_{NP0_{std}}}$. This example illustrates the complexity of assigning Z_i with radiosonde data when several boundary layers interact, and lead to multilayering of the lower troposphere.

In Figure 8b-c, shortly after 13:00 UTC we notice a sudden increase in turbulence up to more than about 2000 m a. g. l. This may be due to another boundary layer advection as the wind direction (see Fig. 8b not shown) suddenly changes from $\sim 200^\circ$ to $\sim 90^\circ$ between ~ 1000 m and ~ 2000 m. A break in the temporal continuity of $NP3$ local maxima is then observed and the imposed growth limit does not allow to follow this sudden evolution. The use of Z_{i_ϵ} (1875 m at 13:15 UTC) allows attributions of $Z_{i_{NP3_{std}}}$ and $Z_{i_{NP0_{std}}}$ to follow this evolution rapid change from 975 m at 13:10 UTC to 1800 m at 13:20 UTC.

From 14:00 UTC onwards, a low-level marine breeze (< 500 m) can be seen on the Fig. 8a and 8b. This marine air is called “La Marinada” in this region (Jimenez et al., 2021), and is typical of the area. It is an entrance of marine air coming from the Mediterranean Sea, which is usually favoured by a continental heat low over northern Spain. Between 15:00 UTC and 16:00 UTC, differences between $Z_{i_{NP3_{std}}}$ and $Z_{i_{NP0_{std}}}$ are observed, showing the high complexity of the atmosphere. After 16:00 UTC, all the attributions are made at 225 m on the first UHF RWP gate. Figure ??h to ??n

Figure 10 shows the data from a radiosonde launched at 18:00 UTC on the same day, where it can be seen that $Z_{i_{NP3_{std}}}$ and $Z_{i_{NP0_{std}}}$ are well established at the height of the maximum potential temperature and mixing ratio gradient. The observed breeze has therefore set up a new convective boundary layer.

At 19:00 UTC, the radiosonde (not shown) data indicate that Z_i decreases below the first reliable RWP gate, CALOTRITON attributions are then overestimated at erroneously overestimated by about 500 m a. g. l.

This example has shown a highly complex situation, which can still occur even in clear sky, and where the conditions. It exemplifies the complexity of automatically assigning Z_i with radiosonde data or remote sensing, when several boundary layers interact and lead to multilayering of the lower troposphere. It also illustrates how the different CALOTRITON attributions can help identifying CBL top, TIBL top, and the advection of internal boundary layers. The flag defined in Sect. 3.3.3 helps to identify the days when this kind of complex layering of the low troposphere may occur.

5 Validation of CALOTRITON with in-situ measurements

The previous sections have shown that $Z_{i_{NP3_{std}}}$ gives the best estimates of Z_i . To validate this result estimate, all CALOTRITON attributions were compared to radiosonde data from the numerous radiosonde data made during the LIAISE and BLLAST campaigns with field experiments, nearby two UHF RWP for each campaign (Table 1). During BLLAST, the CNRM-UHF RWP was installed about 3 km from the P2OA-CRA UHF RWP, at Capvern. In-situ soundings were made two RWP were about 5 km apart, the LAERO UHF RWP at P2OA-CRA and Capvern with balloons (Lothon et al., 2014; Legain et al., 2013) and RPAS (Reuder et al., 2016; Båserud et al., 2020) P2OA-CRA, and the CNRM UHF RWP about 5 km to the South. RPAS (Reuder et al., 2016) profiles were made nearby the two sites, and radiosounding balloons were launched from both sites (Lothon et al., 2014; Legain et al., 2013), a few tens of meters from the RWPs. During LIAISE, the P2OA-LAERO UHF RWP was installed on the a dry area (Els PlanPlans), and the CNRM UHF RWP over the an irrigated area (La Cendrosa) (see Sect. ??4.3), about 15 km away (Boone et al., 2021). Radiosoundings were launched from the two sites. Attribution comparison between $Z_{i_{NP3_{std}}}$ and (a) Z_i from in-situ parcel method, (b) Z_i from in-situ potential temperature gradient method, (c) Z_i from in-situ relative humidity gradient method, (d) Z_i from in-situ mixing ratio gradient method, (e) selected Z_i from in-situ mixing ratio gradient method as described in Sect. ??. For all panels, (grey dashed line) the slope 1/1, the corresponding linear regression (red line) with its characteristics (red text): the number of data points (N), its regression coefficient (R^2), its root mean squared error ($RMSE$), its regression slope (S) and its intercept (I). as well, nearby the RWPs (also a few tens of m). A total of about 500 profiles are available for the evaluation of the CALOTRITON estimates. In-situ profiles are sometimes difficult to interpret, notably in case of complex situations like the example previously discussed (Fig. ??). Therefore, we apply different methods to estimate Z_i from in-situ radiosounding or RPAS profiles. Median filters are applied over the vertical, to the in-situ data to match a vertical resolution of 10 m. The comparison of $Z_{i_{NP3_{std}}}$ with the in-situ estimates, according to the method used to estimate Z_i with in-situ thermodynamical data is shown in Those numerous in situ profiles give the opportunity to evaluate and validate CALOTRITON, but also give some insight on the results from automatic estimates from thermodynamic profiles.

In Fig. 11, and discussed in the following.

Table 5 summarizes the results of the UHF RWP / a and Fig. 11b, we compare $Z_{i_{NP3_{std}}}$ with automatic in-situ comparison with the various CALOTRITON Z_i estimates estimates based respectively on the parcel method (one of the most frequently used), and on the water vapour mixing ratio gradient method (as an example of the gradient methods).

5.0.1 Comparison of CALOTRITON with in-situ parcel method

In the parcel method, a small amount $\delta\theta$ is added to the surface potential temperature (θ_s), and $Z_{i_{parcel}}$ is defined as the height where $\theta = \theta_s + \delta\theta$ above surface (Seibert et al., 2000). In this study Here we set $\delta\theta$ as 0.25°C .

These in-situ Z_i estimates are compared to $Z_{i_{NP3_{std}}}$ results in (Fig. 11a5a). A great disparity of points is observed, which is mainly explained by a poor estimation of $Z_{i_{parcel}}$ in non-textbook cases. They are indeed either overestimated (example in Fig. 22h7a), or underestimated by the potential presence of TIBL (example in Fig. 22a) or by an underestimation of $\delta\theta$; also may not be always appropriate, according to the intensity of the surface layer actual super-adiabatism $\delta\theta$ close to surface.

In addition, a multitude large number of small Z_i estimates by the parcel method (< 200 m) can be observed due to the observation of a positive potential temperature gradient in the very first meters of the profiles. Hennemuth and Lammert (2006) attribute this to evening transitions, but it may actually happen at any time (see Fig. 22h9a), for example by the establishment of local breezes or other advection of stable air masses. type of advection. It can also occur when the surface layer is not clear (showing fluctuations over the vertical) during the start and at the spot of the sounding. The parcel method may or may not be fair in those cases. The in situ radiosounding or RPAS profile is very local and instantaneous. Note that using the bulk Richardson method rather than the parcel method did not significantly change the result of this comparison (not shown). The bulk Richardson Z_i estimates were actually slightly less relevant than the parcel method estimates, with more frequent overestimation of Z_i due to the attribution of Z_i on upper inversions.

5.0.1 Comparison of CALOTRITON with in-situ gradient methods

The in-situ based gradient methods assign Z_i at the height of the strongest gradient of potential temperature, water vapor mixing ratio or relative humidity, below 3000 m. Figure 11b, 11c and 11d show the comparison of those in-situ Z_i estimates with shows the comparison between $Z_{i_{NP3_{std}}}$ and the water vapour mixing ratio gradient estimates. There is a large majority of cases where attributions based on gradient methods water vapour mixing ratio gradient method are largely above $Z_{i_{NP3_{std}}}$. They mostly correspond to attributions to

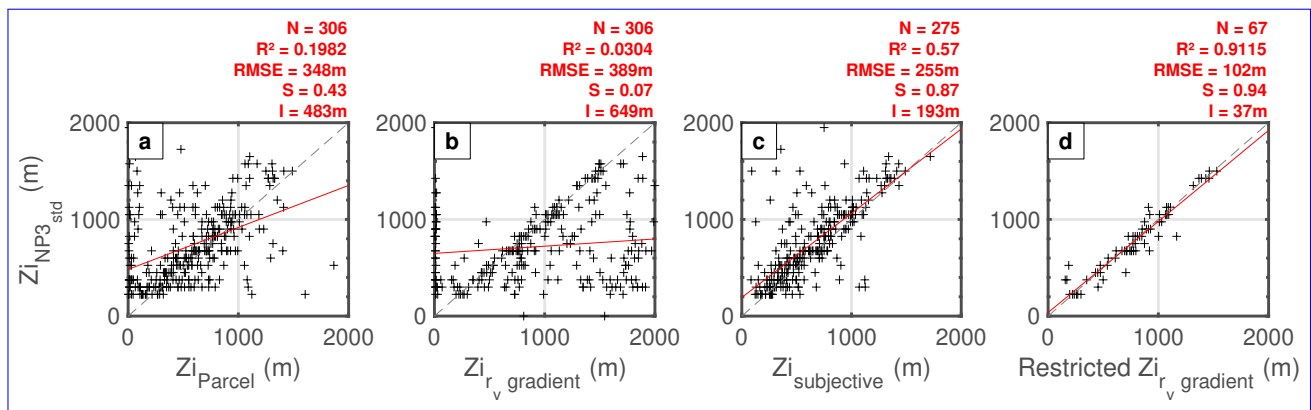


Figure 11. Comparison between $Z_{i_{NP3_{std}}}$ and (a) Z_i from in-situ parcel method, (b) Z_i from in-situ water vapour mixing ratio gradient method, (c) subjective Z_i estimates and (d) restricted Z_i from the convergence of all the in-situ-based estimates. In all panels, the grey dashed line represents the 1/1 slope and the red line is the linear regression. The characteristics of the regression are indicated with the red font text: the number of data points (N), the regression coefficient (R^2), the root mean squared error (RMSE), the regression slope (S) and the intercept (I).

residual layers or upper inversion, as described by Hennemuth and Lammert (2006), and as seen in the previous examples (Fig. 7, Fig. 9). Also a significant number of attributions by gradient methods are very low and correspond to stable surface layer (around morning or evening transitions) ~~as previously stated~~, but also to the fact that ~~we can have one can observe~~ large
585 fluctuations in the surface layer, ~~notably in water vapour mixing ratio, as we can see~~ as seen in Fig. ~~??~~-7b. Similar results are found when considering the potential temperature or the relative humidity for the gradient method (not shown).

~~Thus, Sections ?? and ??~~ Figures 11a and b show that it remains difficult to qualify CALOTRITON estimates with the ~~objective (or at least automatically determined)~~ automatically determined estimates from in-situ parcel ~~and or~~ gradient methods.

590 **5.0.1 Comparison of CALOTRITON with in-situ subjective method**

For this reason, a subjective method of assigning Z_i from in-situ thermodynamical profiles ~~was used. This method remains is~~ helpful. We attempt to keep this method as objective as possible, by assigning Z_i at the height where we observe a first notable discontinuity in the mixing ratio profile associated with discontinuity in the potential temperature profile. The approach is similar to searching for the top of a conserved scalar tracer, and it should also correspond to the height where the entrainment
595 zone starts (see Fig. 1d).

Figure 11e c shows the comparison of ~~these this subjective~~ Z_i ~~obtained by these methods and those done by CALOTRITON using with CALOTRITON estimates based on $NP3_{std}$.~~ We ~~start to have a good concordance~~ obtain a much better agreement between the attributions with ~~the higher a higher~~ regression coefficient ($R^2 = 0.57$), but some points still deviate from the trend and may be due to subjective misinterpretation as we have seen in the presence of TIBL for example, or to failure of
600 CALOTRITON estimates.

5.0.1 Optimized comparison with selected in-situ Z_i

In order to disregard errors in the in-situ estimates, we ~~propose to finally~~ restrict the $Z_{i_{NP3_{std}}}$ / in-situ comparison to the cases where the standard deviation within the estimates from the various in-situ methods is smaller than 100 m. This way, we ensure consistency between those methods, that is, we keep more "simple" or "textbook" situations. We also ensure objectivity.
605 Figure 11e d shows an excellent comparison between $Z_{i_{NP3_{std}}}$ and Z_i from the in-situ mixing ratio gradient method in those conditions, with $R^2 = 0.82$ 0.91 and a root mean squared error ($RMSE$) of ~~152 m that is twice the vertical resolution of the UHF RWP~~ 102 m. However, there are still a few points that depart, which are mainly due to:

- late afternoon conditions, when the atmosphere starts to stabilize in the surface layer. In these cases, we are actually at the limit of the CBL definition;
- 610 – attributions below the UHF RWP vertical detection limitation.

If we ignore in-situ attributions below 225 m and times later than 16:00 UTC, we obtain $R^2 = 0.93$ and $RMSE = 88$ 84 m (that is close to the 75 m UHF RWP vertical resolution), which confirms the consistency of CALOTRITON estimates in those conditions.

Table 5 summarises all the comparisons made between the UHF RWP CALOTRITON estimates (based on various orders of NPx in standard configuration as described in Table 4) and in-situ estimates (based on the different methods). $Zi_{NP4_{std}}$ has a slightly larger R^2 and lower $RMSE$. ~~However when comparing with the subjective in situ Zi estimates. But generally,~~ $NP3_{std}$ -based attributions are very similar to $NP4_{std}$ -based attributions, and moreover lead to 4% additional attributions when compared to the subjective method in-situ estimates. This further supports the optimum choice of using $Zi_{NP3_{std}}$ to estimate Zi with CALOTRITON, and the validity of those estimates. ~~Finally, when we compare the attributions of $NP3_{std}$ with $QF = 1$ with those of restricted Zi_{rv} , which both reflect simple textbook case, the results are excellent with a R^2 of more than 0.96 and an $RMSE = 71$ m, that is lower than the RWP vertical resolution (75 m).~~

Table 5. Summary of linear regression characteristics between Zi from CALOTRITON with NPx ($x = 0$ to 5) in standard configuration as described in Table 4 and Zi from in-situ subjective method, ~~selected restricted Zi from estimates based on~~ in-situ mixing ratio gradient method, ~~agreeing with other in-situ-based estimates~~ as described in ~~Sect. ?? the text~~, and ~~selected same Zi from in-situ mixing ratio gradient method as described in Sect. ?? without taking account with further restrictions (no attributions below 225 m and only before or after 16:00 UTC~~

Compared $Zi_{NPx_{config}}$	$Zi_{NP0_{std}}$	$Zi_{NP1_{std}}$	$Zi_{NP2_{std}}$	$Zi_{NP3_{std}}$	$Zi_{NP4_{std}}$	$Zi_{NP5_{std}}$	$Zi_{NP3_{std}}(flag=1)$ $Zi_{NP3_{std}}$
	with $Zi_{subjective}$						
Number of data points	288	284	286	275	264	254	142
R^2	0.43	0.56	0.47	0.57	0.59	0.56	0.62
$RMSE$	285 m	246 m	309 m	255 m	253 m	270 m	255 m
Slope	0.74	0.85	0.86	0.87	0.89	0.89	0.9
Intercept	219 m	162 m	204 m	193 m	193 m	200 m	150 m
	with restricted $Zi_{rv, gradient}$						
Number of data points	68-70	68-70	69	67	65-66	64-62	61-37-39
R^2	0.67-0.72	0.74-0.80	0.65-0.70	0.82-0.91	0.88	0.88-0.87	0.94
$RMSE$	204-181 m	178-149 m	206-182 m	152-102 m	119-117 m	128-126 m	94-90 m
Slope	0.81-0.84	0.82-0.87	0.76-0.81	0.88-0.94	0.9-0.90	0.93-0.94	0.96
Intercept	81-65 m	95-68 m	162-69 m	71-37 m	81-76 m	56-47 m	45 m
	with restricted $Zi_{rv, gradient}$ without $Zi < 225$ m and only before 16:00 UTC						
Number of data points	52-56	52-56	51-55	49-52	49-52	49	26-29
R^2	0.72-0.70	0.80	0.81	0.82-0.93	0.93	0.94-0.92	0.90-0.96
$RMSE$	184-179 m	144-138 m	139-135 m	88-84 m	82-79 m	109-95 m	80-71 m
Slope	0.99-0.97	0.99	0.99	1.02-1.03	1.02	1.04-1.07	1.02-1.03
Intercept	-86-55 m	-46-38 m	-46-34 m	-39-42 m	-30-33 m	-54-68 m	-47-43 m

~~Finally~~ In conclusion, we have also shown that CALOTRITON is not specific to one UHF RWP and one observational site.

6 Summary and discussion

625 ~~To conclude, we discuss each of the CALOTRITON initial objectives :-~~ With this new algorithm, the main objective of obtaining reliable estimates of Z_i with a UHF RWP, for the analysis of long term series, is met, except for CBL thinner than 225 m here. Such shallow CBL may be currently observed in winter, but also in very strong heat waves or foehn events.

630 ~~(1) To restrict attribution in CBL case: we finally restricted the attribution as little as possible. Only the use of CALOTRITON uses two surface sensors additionally to the RWP : a humidity sensor at 2 m and a threshold value of 90% relative humidity is kept in order to avoid assigning Z_i to the top of stratus returning a strong signal in NPx . The precipitation suppression function based on a threshold in C_n^2 and on the vertical velocity allows to avoid virga, which could not be detected with a rain gauge.~~

635 ~~(2) To manage complex cases: taking into account both the higher reflectivity at inversions and the amount of turbulence within the CBL with the use of NPx allows to improve the attributions in particular in sonic anemometer for the evaluation of the sensible heat flux. We have seen that CALOTRITON can give satisfying results without the sensible heat flux input. The use of the humidity sensor allows to strongly restrict the attributions, especially in the presence of clouds. A choice of $x = 3$ or 4 seems to be the most appropriate. The flag system also allows to better qualify the state of the atmosphere and gives information on the quality and difficulty of the attribution. In complex cases, characterizing the convective boundary layer by a single height may not be appropriate, in particular in the presence of TIBL where it is difficult to determine Z_i , even based on in-situ thermodynamical data. It becomes very difficult to statistically qualify CALOTRITON attributions in such cases. An intercomparison of the results of the StratFinder algorithm (Kotthaus et al., 2020) applied on a newly installed Vaisala CL61 ceilometer at P2OA-CRA with the CALOTRITON estimates is planned in order to better characterize low stratus and fog. It thus remains useful, and a low cost and easy to use input. If this sensor is missing, CALOTRITON will likely attribute inaccurate Z_i attributions by CALOTRITON in complex cases, but also to better understand the differences between the scalar concentration approach, a thermodynamical approach or a turbulence approach in relation with the CBL processes.~~

640 ~~estimates on the top of the fog, when it occurs.~~

645 ~~(3) To respect temporal continuity of Z_i development: although it is not emphasized in this paper, the fact of restricting~~ Relatively to the simpler previously used algorithms for this profiler, and to standard methods, CALOTRITON manages to deal with quite complex cases. Those 'standard methods' are mainly based on catching the appropriate local maximum of C_n^2 with help of temporal continuity. In CALOTRITON, the search for the first attribution of Z_i to at the first reliable

650 ~~UHF RWP gate is a significant progress. Indeed, consistently with Molod et al. (2015) approach. Also taking into account both the higher reflectivity at inversions and the amount of turbulence within the CBL by use of the technique presented by Angevine et al. (1994) assigns Z_i at the height of the maximum reflectivity without taking into account the potential presence of a residual layer in the morning, like is the case in Fig. 8e between 07:00 UTC and 08:00 UTC at about 2500 m. Nevertheless, attribution errors are still observed, essentially in the morning when the residual layers are close to the actual Z_i and the relative threshold of the secondary maximum of NPx (90% before 10:00 UTC) is not sufficient. In contrary, in the afternoon, Z_i usually reaches a plateau. We could have constrained the attributions around the last allocated Z_i and thus avoided taking into account a relative difference between the local maximums of NPx , which adds complexity to the algorithm. However, this choice would not have allowed us to detect the apparition of a new convective boundary layer as we have seen for the LIASIE campaign.~~

660 Finally the empirical choice of growth limit values associated with the relative thresholds of secondary maximum of new key variable NPx gives convincing results. (allows to improve the attributions, in particular in the presence of clouds (x equal 3 or 4) To take into account abrupt seems the most appropriate). This was also found by Bianco and Wilczak (2002) with a different innovative 'fuzzy logic' approach.

The criterium of temporal continuity, which appears as a real need, sometimes induces errors. Indeed, the associated jump threshold that is tolerated for the CBL growth -using- is somehow arbitrary, and prevents the potential abrupt growth in certain conditions. Using Z_{i_ϵ} to allow larger growth limit in those specific conditions helps to better manage complex cases but it was noticed that it can also generate. This is another improvement brought by CALOTRITON. However, this one also can induce errors, in particular in the morning, by attributing Z_i at the height of residual layers. Using an additional median filter on Z_{i_ϵ} makes it possible could allow us to limit these errors by better considering a certain temporal continuity of Z_{i_ϵ} . The choice of a threshold in ϵ for definition of Z_{i_ϵ} estimate is, however, not the most appropriate. An improvement could be brought on that aspect. An intercomparison could also be made between lidar and UHF RWP instruments could itself be improved. It is by itself an interesting useful variable.

(5) To use limited instrumental synergy: only two additional instruments are used in addition to the UHF RWP: a humidity sensor at 2 m and sonic anemometers for the evaluation of the sensible heat flux. The latter could, however, be ignored since the method of searching for the t_{mix} based on the value of C_n^2 at the first gate of the UHF RWP still gives satisfying results. On the other hand, the use of the humidity sensor allows to strongly restrict the attributions, especially in the presence of low stratus and fog, and remains an easy and low cost solution. The set of attributions must also be further restricted, especially when The comparison of CALOTRITON Z_i estimates with in situ thermodynamic profiles has shown that there is no automatic method based on in situ thermodynamic profiles which can deal with the complexity of the atmospheric structure, and that the subjective way remains the best. Such a subjective approach was actually also considered as a reference in Bianco et al. (2008) but applied on the RWP variables.

CALOTRITON is definitely not a simple algorithm, but this actually reveals the need to adapt to the high complexity of the lower atmosphere vertical structure. Bianco et al. (2008) proposed an improved algorithm relative to Bianco and Wilczak (2002) , with more complexity added, which demonstrates this need of complexity and adjustments, to optimize the understanding and detection of the appropriate interface. The flag system and various types of Z_i gets below the RWP lower vertical limit, when the boundary layer initiates its night transition. Moreover, sensible heat flux data can be used to only keep the estimates of Z_i in the estimates proposed in CALOTRITON allow us to express and document this vertical structure complexity, and meanwhile give information on the quality and difficulty of the Z_i estimations. In complex cases, characterizing the convective boundary layer by a single height may actually not be appropriate, in particular in the presence of positive flux. However, this choice has not been made at P2OA-CRA, whose location at the foot of the Pyrenees is subject to Foehn winds, potentially resulting in daytime negative sensible heat flux measurements (but positive latent heat flux) in the surface layer TIBL where it is difficult to determine (and even define) Z_i , even based on in-situ thermodynamical data. It becomes very difficult to statistically qualify CALOTRITON attributions in such cases. Over the 8-year time series of the UHF RWP at P2OA, we find that 17% of the days have more than 75% of their Z_i estimates with $QF=1$. This means that about 17% of the days are quite close to textbook cases,

685
690

with large confidence on CALOTRITON Z_i estimates. In contrast, at Els Plans during the LIAISE campaign, none of the days presents $QF=1$ for more than 75% of the time of day. That is there is no simple textbook case in this area during the LIAISE campaign summer.

~~We have not addressed so far the difficulty of attribution of~~ The use of the different Z_i estimates by CALOTRITON is also of large interest for documenting the complex structure of the CBL. Though a statistical use should be done only with caution. One can for example estimate the occurrence of significant differences between $Z_{i_{NP3_{std}}}$ and $Z_{i_{NP3_{sub}}}$. At P2OA during the winter period, which will be primarily due to small Z_i , often below the lower detection limit of 8-year time series, we find that only 3% of the days show a significant difference between both estimates for more than 25% of the UHF RWP, but also to reduced cover range of the RWP in a much drier atmosphere. The choice of dividing the NPx by the profile mean initially aimed at working with dimensionless variable but also at applying this algorithm to uncalibrated UHF RWP reflectivities. It remains interesting to regularly calibrate it, in order to optimize the threshold of C_n^2 for the precipitation periods removal.

Finally, the main objective of obtaining reliable estimates of Z_i with a UHF RWP, for the analysis of long term series, is mettime. This would mean that TIBL are not very frequent at P2OA. In contrast, at Els Plan during LIAISE, we find 26% of such days, which likely means that TIBL occurs very frequently during the LIAISE campaign. One can also estimate the occurrence of differences between $Z_{i_{NP3_{std}}}$ and $Z_{i_{NP0_{inv}}}$: At P2OA, over the 8-year time series, 72% of the days show a significant difference between both for more than 25% of the time of day. Those days can be related to the large occurrence of cloud layers above the CBL top which generate an inversion. At Els Plans during LIAISE, this number reaches 92%, which likely means that there are established upper inversions in the LIAISE area. Those preliminary statistics reveal the high complexity of the LIAISE study area, and the potential of the CALOTRITON various estimates and flags. However, case by case studies and further analyses are needed to help us qualifying this potentiality.

Code availability.

CALOTRITON code is available from the authors upon request.

Data availability.

~~Table 1 summarises the data availability. Only the 6 draws the list of available dataset, with DOI and references.~~ The CT25k ceilometer data are available from the authors upon request.

Author contributions.

AP is the main author of CALOTRITON algorithm: conception, coding, tests, evaluation, data analysis. He is also the main writer of the article. ML supervised the work and analysis, and helped in the writing. She is the principal investigator of the

Table 6. [Summary of instruments used and datasets](#)

Instrument	Context	Location	Period	DOI Reference
LAERO UHF RWP	P2OA	Campistrous, France	2015-2022	Lothon et al. (to be specified)
LAERO UHF RWP	BLLAST	Campistrous, France	June - July 2011	Saïd (2012)
LAERO UHF RWP	LIAISE	Els Plans, Spain	July 2021	Lothon and Vial (2022)
CNRM UHF RWP	BLLAST	Capvern, France	June to July 2011	Garrouste (2011)
CNRM UHF RWP	LIAISE	La Cendrosa, Spain	July 2021	Vial (2023)
CT25k Ceilometer	P2OA	Campistrous, France	2016-2019	Contact Author
Sonic anemometer	P2OA	Campistrous, France	2015-2022	Lohou et al. (to be specified), t)
Sonic anemometer	BLLAST	Campistrous, France	June to July 2011	Lohou (2017)
Sonic anemometer	LIAISE	Els Plans, Spain	July 2021	Price (2023a)
Sonic anemometer	LIAISE	LA Cendrosa, Spain	July 2021	Canut et al. (2022)
Radiosoundings	BLLAST	Campistrous, France	June to July 2011	Lothon (2018)
Radiosoundings	BLLAST	Capvern, France	June to July 2011	Legain (2011)
Radiosoundings	LIAISE	Els Plans, Spain	July 2021	Price (2023b)
Radiosoundings	LIAISE	La Cendrosa, Spain	July 2021	Garrouste et al. (2022)
RPAS	BLLAST	Campistrous, France	June to July 2011	Reuder and Jonassen (2017)

[P2OA-LAERO](#) UHF RWP. JA and PYM are the coordinators of the funding contract, and collaborated to the work. BC is the author of the initial code for the UHF RWP data process, and of the previous algorithm for Zi estimates. He helped to the algorithm conception. SD is responsible for the P2OA-CRA instrumentation and data. She and AV helped in instrumentation maintenance, data process, and data availability. YB operates the [P2OA UHF RWP](#), and helped [LAERO UHF RWP at P2OA and during field experiments, and helped](#) in the operation of the CNRM UHF RWP during LIAISE. FL is the principal investigator of the 60 m tower, and contributed to the writing. GC was the lead of the instrumental deployment during LIAISE, especially of the CNRM instruments installed at La Cendrosa. JB was responsible for the deployment of radiosoundings at Els [Plan-Plans](#) during LIAISE, and contributed to the writing. JR was the PI of SUMO RPAS during BLLAST, and contributed to the writing.

730 *Competing interests.*

The contact author has declared that neither of the authors has any competing interests.

Acknowledgements. We gratefully acknowledge the French Atomic Energy Commission (CEA) assisted by the Université Paul Sabatier, Toulouse, for funding this study and their support.

735 P2OA-CRA observation data were collected at the Pyrenean Platform for Observation of the Atmosphere P2OA (<http://p2oa.aero.obs-mip.fr>). P2OA facilities and staff are funded and supported by the University Paul Sabatier Toulouse 3, France, and CNRS (Centre National de la Recherche Scientifique). P2OA is a component of the ACTRIS-Fr Research Infrastructure and benefits from AERIS data centre (<https://www.aeris-data.fr/>) for hosting service data. The 60 m tower is partly supported by the POCTEFA/FLUXPYR European program.

The BLLAST field experiment was made possible thanks to the contribution of several institutions and supports : INSU-CNRS (Institut National des Sciences de l'Univers, Centre national de la Recherche Scientifique, LEFE-IDAO program), Météo-France, Observatoire Midi-

740 Pyrénées (University of Toulouse), EUFAR (EUropean Facility for Airborne Research) and COST ES0802 (European Cooperation in the field of Scientific and Technical). The field experiment would not have occurred without the contribution of all participating European and American research groups, which all have contributed in a significant amount (see <https://bllast.aeris-data.fr/bllast-supports/>). The BLLAST field experiment was hosted by the instrumented site of Centre de Recherches Atmosphériques, [LannemezanCampistrous](#), France (Observatoire Midi-Pyrénées, Laboratoire d'Aérodologie). BLLAST data are managed by SEDOO, from Observatoire Midi-Pyrénées. The French

745 ANR (Agence Nationale de la Recherche) supported BLLAST analysis in the 2013-2015 BLLAST-A project. The french contribution to the LIAISE project has been supported by ANR HILIAISE and Meteo-France. We acknowledge Gilles André, Géraldine Pagan, Vinciane Unger, Alain Dabas, Alexandre Paci, and GMEI/LISA team of CNRM UMR. We also acknowledge Jeremy Price and all the Met Office team involved in LIAISE.

[The contribution of Joachim Reuder to this study was partially funded by the project LOWT, funded by the Research Council of Norway \(RCN\) under project number 325294.](#)

750

References

- Angevine, W. M.: Atmospheric boundary layer height measurements with wind profilers: Successes and cautions, *International Geoscience and Remote Sensing Symposium (IGARSS)*, 1, 197–198, <https://doi.org/10.1109/igarss.2000.860466>, 2000.
- 755 Angevine, W. M., White, A. B., and Avery, S. K.: Boundary-layer depth and entrainment zone characterization with a boundary-layer profiler, *Boundary-Layer Meteorology*, 68, 375–385, <https://doi.org/10.1007/BF00706797>, 1994.
- Bianco, L. and Wilczak, J. M.: Convective boundary layer depth: Improved measurement by Doppler radar wind profiler using fuzzy logic methods, *Journal of Atmospheric and Oceanic Technology*, 19, 1745–1758, [https://doi.org/10.1175/1520-0426\(2002\)019<1745:CBLDIM>2.0.CO;2](https://doi.org/10.1175/1520-0426(2002)019<1745:CBLDIM>2.0.CO;2), 2002.
- 760 Bianco, L., Wilczak, J. M., and White, A. B.: Convective boundary layer depth estimation from wind profilers: Statistical comparison between an automated algorithm and expert estimations, *Journal of Atmospheric and Oceanic Technology*, 25, 1397–1413, <https://doi.org/10.1175/2008JTECHA981.1>, 2008.
- Blay-Carreras, E., Pino, D., Arellano, J. V.-G. D., Boer, A. V. D., Coster, O. D., Darbieu, C., Hartogensis, O., Lohou, F., Lothon, M., and Pietersen, H.: Role of the residual layer and large-scale subsidence on the development and evolution of the convective boundary layer, *Atmospheric Chemistry and Physics*, 14, 4515–4530, <https://doi.org/10.5194/acp-14-4515-2014>, 2014.
- 765 Boone, A., Bellvert, J., Best, M., Brooke, J., Canut-Rocafort, G., Cuxart, J., Hartogensis, O., Le Moigne, P., Miró, J. R., Polcher, J., Price, J., Quintana Seguí, P., and Wooster M.: Updates on the international Land Surface Interactions with the Atmosphere over the Iberian Semi-Arid Environment (LIAISE) Field Campaign, *Gewex News*, 31(4), 17–21, 2021.
- Båserud, L., Reuder, J., Jonassen, M. O., Bonin, T. A., Chilson, P. B., Jiménez, M. A., and Durand, P.: Potential and Limitations in Estimating Sensible-Heat-Flux Profiles from Consecutive Temperature Profiles Using Remotely-Piloted Aircraft Systems, *Boundary-Layer Meteorology*, 174, 145–177, <https://doi.org/10.1007/s10546-019-00478-9>, 2020.
- 770 Caicedo, V., Rappenglück, B., Lefer, B., Morris, G., Toledo, D., and Delgado, R.: Comparison of aerosol lidar retrieval methods for boundary layer height detection using ceilometer aerosol backscatter data, *Atmospheric Measurement Techniques*, 10, 1609–1622, <https://doi.org/10.5194/amt-10-1609-2017>, 2017.
- Canut, G., Garroute, O., and Etienne, J.-C.: LIAISE LA-CENDROSA CNRM MTO-1MIN L2. [DataSet], <https://doi.org/https://doi.org/10.25326/33>, 2022.
- 775 Cohn, S. A. and Angevine, W. M.: Boundary Layer Height and Entrainment Zone Thickness Measured by Lidars and Wind-Profiling Radars, *Journal of Applied Meteorology*, 39, 1233–1247, [https://doi.org/10.1175/1520-0450\(2000\)039<1233:BLHAEZ>2.0.CO;2](https://doi.org/10.1175/1520-0450(2000)039<1233:BLHAEZ>2.0.CO;2), 2000.
- Collaud Coen, M., Praz, C., Haeefe, A., Ruffieux, D., Kaufmann, P., and Calpini, B.: Determination and climatology of the planetary boundary layer height above the Swiss plateau by in situ and remote sensing measurements as well as by the COSMO-2 model, *Atmospheric Chemistry and Physics*, 14, 13 205–13 221, <https://doi.org/10.5194/acp-14-13205-2014>, 2014.
- 780 Compton, J. C., Delgado, R., Berkoff, T. A., and Hoff, R. M.: Determination of planetary boundary layer height on short spatial and temporal scales: A demonstration of the covariance wavelet transform in ground-based wind profiler and lidar measurements, *Journal of Atmospheric and Oceanic Technology*, 30, 1566–1575, <https://doi.org/10.1175/JTECH-D-12-00116.1>, 2013.
- Couvreux, F., Bazile, E., Canut, G., Seity, Y., Lothon, M., Lohou, F., Guichard, F., and Nilsson, E.: Boundary-layer turbulent processes and mesoscale variability represented by numerical weather prediction models during the BLLAST campaign, *Atmospheric Chemistry and Physics*, 16, 8983–9002, <https://doi.org/10.5194/acp-16-8983-2016>, 2016.
- 785

- Davis, K. J., Gamage, N., Hagelberg, C., Kiemle, C., Lenschow, D., and Sullivan, P.: An objective method for deriving atmospheric structure from airborne lidar observations, *Journal of Atmospheric and Oceanic Technology*, 17, 1455–1468, 2000.
- 790 Dearnoff, J. W.: Theoretical expression for the countergradient vertical heat flux, *Journal of Geophysical Research*, 77, 5900–5904, <https://doi.org/10.1029/jc077i030p05900>, 1972.
- Doviak, R. and Zrnic, D.: *Doppler Radar and Weather Observations*, Elsevier, <https://doi.org/10.1016/C2009-0-22358-0>, 1993.
- Duncan, J. B., Bianco, L., Adler, B., Bell, T., Djalalova, I. V., Riihimaki, L., Sedlar, J., Smith, E. N., Turner, D. D., Wagner, T. J., and Wilczak, J. M.: Evaluating convective planetary boundary layer height estimations resolved by both active and passive remote sensing instruments during the CHEESEHEAD19 field campaign, *Atmospheric Measurement Techniques*, 15, 2479–2502, <https://doi.org/10.5194/amt-15-2479-2022>, 2022.
- 795 Durand, P., Druilhet, A., and Briere, S.: A Sea-Land Transition Observed during the COAST Experiment, *Journal of the Atmospheric Sciences*, 46, 96–116, [https://doi.org/10.1175/1520-0469\(1989\)046<0096:ASLTOD>2.0.CO;2](https://doi.org/10.1175/1520-0469(1989)046<0096:ASLTOD>2.0.CO;2), 1989.
- Frehlich, R., Meillier, Y., Jensen, M. L., Balsley, B., and Sharman, R.: Measurements of Boundary Layer Profiles in an Urban Environment, *Journal of Applied Meteorology and Climatology*, 45, 821–837, <https://doi.org/10.1175/JAM2368.1>, 2006.
- 800 Garrouste, O.: UHF CNRM Site 2. [Dataset], <https://doi.org/https://doi.org/10.6096/blast.uhf.site2>, 2011.
- Garrouste, O., Canut, G., and Roy, A.: LIAISE LA-CENDROSA CNRM RS L2. [Dataset]., <https://doi.org/https://doi.org/10.25326/322>, 2022.
- Grimsdell, A. W. and Angevine, W. M.: Convective boundary layer height measurement with wind profilers and comparison to cloud base, *J. Atmos. Oceanic Technol.*, 15, 1331–1338, 1998.
- 805 Grimsdell, A. W., , and Angevine, W. M.: Observations of the Afternoon Transition of the Convective Boundary Layer, *JOURNAL OF APPLIED METEOROLOGY*, 41, 3–11, 2002.
- Haefelin, M., Angelini, F., Morille, Y., Martucci, G., Frey, S., Gobbi, G. P., Lolli, S., O’Dowd, C. D., Sauvage, L., Xueref-Rémy, I., Wastine, B., and Feist, D. G.: Evaluation of Mixing-Height Retrievals from Automatic Profiling Lidars and Ceilometers in View of Future Integrated Networks in Europe, *Boundary-Layer Meteorology*, 143, 49–75, <https://doi.org/10.1007/s10546-011-9643-z>, 2012.
- 810 Hanna, S. R.: The thickness of the planetary boundary layer, *Atmos. Environ.*, 3, 519–536, 1969.
- Hennemuth, B. and Lammert, A.: Determination of the atmospheric boundary layer height from radiosonde and lidar backscatter, *Boundary-Layer Meteorology*, 120, 181–200, <https://doi.org/10.1007/s10546-005-9035-3>, 2006.
- Heo, B.-H., Jacoby-Koaly, S., Kim, K.-E., Campistron, B., Benech, B., and Jung, E.-S.: Use of the Doppler Spectral Width to Improve the Estimation of the Convective Boundary Layer Height from UHF Wind Profiler Observations, 2000.
- 815 Heo, B. H., Jacoby-Koaly, S., Kim, K. E., Campistron, B., Benech, B., and Jung, E. S.: Use of the Doppler spectral width to improve the estimation of the convective boundary layer height from UHF wind profiler observations, *Journal of Atmospheric and Oceanic Technology*, 20, 408–424, [https://doi.org/10.1175/1520-0426\(2003\)020<0408:UOTDSW>2.0.CO;2](https://doi.org/10.1175/1520-0426(2003)020<0408:UOTDSW>2.0.CO;2), 2003.
- Holzworth, G. C.: Estimates of mean maximum mixing depths in the contiguous united states, *Monthly Weather Review*, 92, 235–242, [https://doi.org/10.1175/1520-0493\(1964\)092<0235:EOMMMD>2.3.CO;2](https://doi.org/10.1175/1520-0493(1964)092<0235:EOMMMD>2.3.CO;2), 1964.
- 820 Jacoby-Koaly, S.: Application d’un radar profileur de vent UHF à l’étude de la couche limite atmosphérique, Ph.D. thesis, <http://www.theses.fr/2000TOU30144>, thèse de doctorat dirigée par Campistron, Bernard Physique de l’atmosphère Toulouse 3 2000, 2000.
- Jacoby-Koaly, S., Campistron, B., Bernard, S., Bénech, B., Arduin-Girard, F., Dessens, J., Dupont, E., and Carissimo, B.: Turbulent Dissipation Rate In The Boundary Layer Via UHF Wind Profiler Doppler Spectral Width Measurements, *Boundary-Layer Meteorology*, 103, 361–389, <https://doi.org/10.1023/A:1014985111855>, 2002.

- 825 Jimenez, M.-A., Grau, A., Martínez-Villagrasa, D., and Cuxart, J.: Characterisation of the marine-air intrusion Marinada in the eastern Ebro subbasin, Under revision at the International Journal of Meteorology, 2021.
- Kossmann, M., Gtlin, R. V., Corsmeier, U., Vogel, B., Fiedler, F., Binder, H.-J., Kalthoff, N., and Beyrich, F.: Aspects of the convective boundary layer structure over complex terrain, *Atmospheric Environment*, 32, 1323–1348, 1998.
- Kotthaus, S., Haeffelin, M., Drouin, M. A., Dupont, J. C., Grimmond, S., Haeffele, A., Hervo, M., Poltera, Y., and Wiegner, M.: Tailored
830 algorithms for the detection of the atmospheric boundary layer height from common automatic lidars and ceilometers (Alc), *Remote Sensing*, 12, 1–23, <https://doi.org/10.3390/rs12193259>, 2020.
- Kotthaus, S., Bravo-Aranda, J. A., Collaud Coen, M., Guerrero-Rascado, J. L., Costa, M. J., Cimini, D., O'Connor, E. J., Hervo, M., Alados-Arboledas, L., Jiménez-Portaz, M., Mona, L., Ruffieux, D., Illingworth, A., and Haeffelin, M.: Atmospheric boundary layer height from ground-based remote sensing: a review of capabilities and limitations, *Atmospheric Measurement Techniques*, 16, 433–479,
835 <https://doi.org/10.5194/amt-16-433-2023>, 2023.
- Legain, D.: Frequent radiosoundings Site 2. [Dataset], <https://doi.org/https://doi.org/10.6096/bllast.frequentsoundingsite2>, 2011.
- Legain, D., Bousquet, O., Douffet, T., Tzanos, D., Moulin, E., and Barrie, J.: High-frequency boundary layer profiling with reusable radiosondes, *Atmospheric Measurement Techniques*, 6, 2195–2205, <https://doi.org/10.5194/amt-6-2195-2013>, 2013.
- Liu, Z., Barlow, J. F., Chan, P.-W., Fung, J., Li, Y., Ren, C., Mak, H., and Ng, E.: A Review of Progress and Applications of Pulsed Doppler
840 Wind LiDARs, *Remote Sens.*, 11, 2522, 2019.
- Lohou, F.: Meteorological parameters and flux. [Dataset], <https://doi.org/https://doi.org/10.6096/bllast.60mtower.meteo>, 2017.
- Lohou, F., Derrien, S., and Vial, A.: [Dataset], <https://doi.org/to be specified, to be specifieda>.
- Lohou, F., Derrien, S., and Vial, A.: to be specified, [Dataset], <https://doi.org/to be specified, to be specifiedb>.
- Lothon, M.: MODEM Radiosoundings Site 1. [Dataset], <https://doi.org/https://doi.org/10.6096/bllast.modem>, 2018.
- 845 Lothon, M. and Vial, A.: LIAISE ELS-PLANS LAERO UHFWindProfiler-LowMode L2. [Dataset], <https://doi.org/https://doi.org/10.25326/363>, 2022.
- Lothon, M., Lenschow, D. H., and Mayor, S. D.: Coherence and scale of vertical velocity in the convective boundary layer from a Doppler lidar, *Boundary-Layer Meteorology*, 121, 521–536, <https://doi.org/10.1007/s10546-006-9077-1>, 2006.
- Lothon, M., Lohou, F., Pino, D., Couvreux, F., Pardyjak, E. R., Reuder, J., Arellano, J. V.-G. D., Durand, P., Hartogensis, O., Legain, D.,
850 Augustin, P., Gioli, B., Lenschow, D. H., Faloon, I., Yagüe, C., Alexander, D. C., Angevine, W. M., Bargain, E., Barrié, J., Bazile, E., Bezombes, Y., Blay-Carreras, E., Boer, A. V. D., Boichard, J. L., Bourdon, A., Butet, A., Campistron, B., Coster, O. D., Cuxart, J., Dabas, A., Darbieu, C., Deboudt, K., Delbarre, H., Derrien, S., Flament, P., Fourmentin, M., Garai, A., Gibert, F., Graf, A., Groebner, J., Guichard, F., Jiménez, M. A., Jonassen, M., Kroonenberg, A. V. D., Magliulo, V., Martin, S., Martinez, D., Mastroiello, L., Moene, A. F., Molinos, F., Moulin, E., Pietersen, H. P., Pignatelli, B., Pique, E., Román-Cascón, C., Rufin-Soler, C., Saïd, F., Sastre-Marugán, M., Seity, Y., Steeneveld,
855 G. J., Toscano, P., Traullé, O., Tzanos, D., Wacker, S., Wildmann, N., and Zaldei, A.: The BLLAST field experiment: Boundary-Layer late afternoon and sunset turbulence, *Atmospheric Chemistry and Physics*, 14, 10931–10960, <https://doi.org/10.5194/acp-14-10931-2014>, 2014.
- Lothon, M., Gheusi, F., Lohou, F., Pont, V., Derrien, S., Bezombes, Y., Leclerc, E., Vial, A., Athier, G., Jambert, C., Gardrat, E., Andriatiana, A., Meyerfeld, Y., Campistron, B., Saïd, F., Philibert, A., Stark, F., Estrampes, J.-B., Pique, E., Guesdon, F., Bret, G., Lacassagne, F.,
860 Guesdon, L., Gueffier, J., Jeroen, S., and Zaïda, G. K.: The long-term dataset of the Pyrenean Platform for Observation of the Atmosphere, To be submitted to *Earth System Science Data*, 2023.
- Lothon, M., Bezombes, Y., and Vial, A.: to be specified [Dataset], <https://doi.org/to be specified, to be specified>.

- Min, J. S., Park, M. S., Chae, J. H., and Kang, M.: Integrated System for Atmospheric Boundary Layer Height Estimation (ISABLE) using a ceilometer and microwave radiometer, *Atmospheric Measurement Techniques*, 13, 6965–6987, <https://doi.org/10.5194/amt-13-6965-2020>, 2020.
- 865 Molod, A., Salmun, H., and Dempsey, M.: Estimating planetary boundary layer heights from NOAA Profiler Network wind profiler data, *Journal of Atmospheric and Oceanic Technology*, 32, 1545–1561, <https://doi.org/10.1175/JTECH-D-14-00155.1>, 2015.
- Nilsson, E., Lohou, F., Lathon, M., Pardyjak, E., Mahrt, L., and Darbieu, C.: Turbulence kinetic energy budget during the afternoon transition - Part 1: Observed surface TKE budget and boundary layer description for 10 intensive observation period days, *ATMOSPHERIC CHEMISTRY AND PHYSICS*, 16, 8849–8872, <https://doi.org/10.5194/acp-16-8849-2016>, 2016a.
- 870 Nilsson, E., Lathon, M., Lohou, F., Pardyjak, E., Hartogensis, O., and Darbieu, C.: Turbulence kinetic energy budget during the afternoon transition - Part 2: A simple TKE model, *ATMOSPHERIC CHEMISTRY AND PHYSICS*, 16, 8873–8898, <https://doi.org/10.5194/acp-16-8873-2016>, 2016b.
- Pino, D., Jonker, H. J. J., Arellano, J. V.-G. D., and Dosio, A.: Role of Shear and the Inversion Strength During Sunset Turbulence Over Land: Characteristic Length Scales, *Boundary-Layer Meteorology*, 121, 537–556, <https://doi.org/10.1007/s10546-006-9080-6>, 2006.
- 875 Price, J.: LIAISE ELS-PLANS UKMO MTO-30MIN L2. [Dataset]., <https://doi.org/https://doi.org/10.25326/430>, 2023a.
- Price, J.: LIAISE ELS-PLANS UKMO radiosondes L1. [Dataset]., <https://doi.org/https://doi.org/10.25326/429>, 2023b.
- Reuder, J. and Jonassen, M.: SUMO. [Dataset]., <https://doi.org/https://doi.org/10.25326/469>, 2017.
- Reuder, J., Båserud, L., Jonassen, M. O., Kral, S. T., and Müller, M.: Exploring the potential of the RPA system SUMO for multipurpose boundary-layer missions during the BLLAST campaign, *Atmospheric Measurement Techniques*, 9, 2675–2688, <https://doi.org/10.5194/amt-9-2675-2016>, 2016.
- 880 Saïd, F.: LA Site 1. [Dataset], <https://doi.org/https://doi.org/10.6096/bllast.uhf.site1>, 2012.
- Seibert, P., Beyrich, F., Gryning, S.-E., Joffre, S., Rasmussen, A., and Tercier, P.: Review and intercomparison of operational methods for the determination of the mixing height, *Atmospheric environment*, 34, 1001–1027, 2000.
- 885 Stull, R. B.: *An Introduction to Boundary Layer Meteorology*, Springer Netherlands, <https://doi.org/10.1007/978-94-009-3027-8>, 1988.
- Turner, D. D. and Lohnert, U.: Ground-based temperature and humidity profiling: Combining active and passive remote sensors, *Atmospheric Measurement Techniques*, 14, 3033–3048, <https://doi.org/10.5194/amt-14-3033-2021>, 2021.
- Vial, A.: to be specified, <https://doi.org/to be specified>, 2023.
- Wadteufel, P. and Corbin, H.: On the analysis of single-Doppler data, *J. App. Meteor.*, 18, 523–542, 1979.
- 890 White, A. B.: Mixing Depth Detection Using 915-MHz Radar Reflectivity Data, *Proceedings of the 8th Symposium on Meteorological Observations and Instrumentation*, Anaheim, CA, American Meteorological Society, 45 Beacon St., Boston, MA, p. 248–250, 1993.